The Impact of Varying Environmental Conditions on the Spatial and Temporal Patterns of Orographic Precipitation over the Pacific Northwest near Portland, Oregon

SANDRA E. YUTER, DAVID A. STARK, JUSTIN A. CROUCH, AND M. JORDAN PAYNE

North Carolina State University, Raleigh, North Carolina

BRIAN A. COLLE

Stony Brook University, Stony Brook, New York

(Manuscript received 16 November 2009, in final form 31 October 2010)

ABSTRACT

Operational radar data from three winter seasons (2003–06) in Portland, Oregon, in the U.S. Pacific Northwest are used to describe how orographic precipitation varies with cross-barrier wind speed, 0°C level height, and stability over the moderately wide (~50-km half-width) Cascade Mountain Range. Orographic enhancement is specified in terms of location, frequency, and relative intensity of the reflectivity (precipitation field). The typical storm for the region, as defined by the 25th to 75th percentile characteristics, is compared to storms with <25th and >75th percentile characteristics for a given variable. About half of Portland-region storms have a low-level wind direction within a relatively narrow azimuth range. This subset of storms is used to examine the sensitivity of orographic enhancement relative to other environmental variables. Cross-barrier wind speed has a stronger role in determining the magnitude of precipitation frequency than either 0°C level or stability. Cross-barrier wind speed and 0°C level height have separate but comparable roles in determining the frequency of relatively heavier precipitation. The increase in precipitation frequency with stronger cross-barrier wind speed is partially attributed to the higher occurrence of intermittent convective cells intersecting the slope. The area where inferred riming growth occurs over local peaks on the windward slope broadens upslope as the 0°C level height increases. In the Portland region, variations in the squared moist Brunt–Väisälä frequency yield smaller differences in the pattern and intensity of precipitation enhancement than either cross-barrier wind speed or 0°C level height.

1. Introduction

Much progress has been made in the last decade in the study of orographic precipitation using high-resolution idealized and forecast models, case studies from field projects, and the analysis of radar and precipitation-gauge characteristics from multiseason datasets. Mountains more commonly modify and amplify precipitation associated with preexisting weather disturbances rather than solely initiating all the precipitation (Smith 2006). For unblocked flow, the strength and depth of ascent over the windward slope depends on the size and shape of the barrier, the wind speed, and the stability of the flow as given by the linear gravity wave theory (Colle 2004; Smith and Barstad 2004; Kunz and Kottmeier 2006). Jiang (2003) found that, within some orographic flows, the release of latent heat due to condensation can cause low-level air to ascend up to twice the height of dry air. Smith (2003) and Smith and Barstad (2004) developed a linear model that scales precipitation proportional to the combination of terrain slope, cross-barrier flow, and column-integrated moisture with modifications by advective processes and wave dynamics. Smith et al. (2005) used this model to reproduce the east–west pattern of precipitation gradients across Oregon. Hughes et al. (2009) found that such linear models agree closely with observations for unblocked flow but degrade in performance for blocked-flow cases.

The enhancement of precipitation above or near local peaks in terrain by gravity waves has been examined in

Corresponding author address: Dr. Sandra E. Yuter, Dept. of Marine, Earth, and Atmospheric Sciences, North Carolina State University, Raleigh, NC 27695.
E-mail: seyuter@ncsu.edu

DOI: 10.1175/2010JHM1239.1

several recent observation and modeling studies (Colle 2004; Colle et al. 2005a,b; Garvert et al. 2005a,b; Doyle and Jiang 2006; Garvert et al. 2007; Colle 2008). For example, Minder et al. (2008) found a persistent mean pattern of precipitation enhancement ~10 km wide over the ~800 m high ridges of the western slope of the Olympic Mountains in Washington using precipitation-gauge observations and mesoscale model output. Analysis of vertically pointing radar data from the European Alps and Oregon Cascades has suggested that turbulence within a layer of strong shear along the windward slope could enhance precipitation growth and fallout (Houze and Medina 2005). Kirshbaum and Durran (2005) found that both local terrain peaks and low-amplitude random topographic roughness were effective at organizing and fixing the location of orographic rainbands.

Intensive analysis of observations and modeling studies from the Mesoscale Alpine Programme (MAP; Bougeault et al. 2001) and the Improvement of Microphysical Parameterization through Observational Verification Experiment II (IMPROVE II; Stoelinga et al. 2003) field programs have led to refinements of conceptual models of orographic enhancement. In particular, these studies clarified the superposition of orographic enhancement mechanisms from the mean upslope flow and the smaller-scale topographic gravity wave over terrain. In both stable and unstable flows, preexisting small-scale cellularity is often enhanced upstream and along the windward slopes of the mountain barriers (Smith et al. 2003; Rotunno and Houze 2007). A terrain parallel cross section over the Cascades shown in Garvert et al. (2007, their Figs. 5 and 14) indicates a complex pattern of ridge-scale upward motions and precipitation enhancement during a strong cross-barrier flow event (~30 m s^{-1} at crest level). For a weaker cross-barrier flow event (15 m s^{-1} at 1.75 km MSL) and weaker stability, there was less correlation between the locations of precipitation maxima and upward motion over the ridges (Colle et al. 2008).

There have been a few studies that have used ground-based radar over an extended period to explore the variations in orographic precipitation. For example, James and Houze (2005, hereafter referred to as JH2005) used operational radar data obtained from 61 heavy precipitation days from Eureka, California, along the coast of northern California. They found both upstream precipitation enhancement extending 60 km upwind from the coastline (within 150 km from the crest of the Coastal Range) and over the first two peaks in terrain for winter storms. JH2005 found that orographic enhancement was more pronounced under joint conditions when the midlevel (500–700 hPa) flow was strong (>30 m s^{-1}), midlevel dewpoint depression was low (<3°C), low-level (900–800 hPa) wind speed was > 20 m s^{-1}, and low-level stability was > 0 s^{-1}.

Panziera and Germann (2010, hereafter referred to as PG2010) examined 58 long-lived, widespread precipitation events in the Southern Alps to determine a heuristic framework for nowcasting orographic precipitation events. They found that the direction of the wind determined the locations of precipitation and that upstream wind velocity had a larger impact on the intensity and frequency of precipitation compared to variations in moist static stability. In their large sample of heavy precipitation events from January 2004 to December 2008, flows with Froude number (Fr) < 1 did not typically exhibit the degree of enhancement of precipitation upwind of the barrier described in Houze et al. (2001), which considered all precipitation events during the 1998 and 1999 autumn seasons.

For hydrological and climate applications, a key parameter is the surface precipitation accumulation. Most precipitation, including orographic precipitation, is usually intermittent and discontinuous in space. The relative importance of diverse processes associated with 0.5 mm h^{-1} rainfall for 5 h may differ from those associated 2.5 mm h^{-1} rainfall for 1 h. To better understand the underlying processes, we follow Rotunno and Ferretti (2001) and decompose precipitation accumulation into intensity and frequency. The surface precipitation accumulation (A) at a specific location can be described as the sum of precipitation rates (R) times their durations (t) over the period under study:

$$A = \sum_i R_i t_i. \tag{1}$$

For the simplified situation in which there is no ice, the R is proportional to the vertical motion of the assumed saturated airflow (Smith 1979; Rotunno and Ferretti 2001). Higher surface air temperature under these saturated conditions increases the precipitable water (Miglietta and Rotunno 2006). However, the presence of ice, particularly graupel, when freezing levels are near crest height can augment surface rainfall such that the highest surface temperatures do not necessarily have the maximum rain rates (Miglietta and Rotunno 2006).

This study uses operational radar and upper-air sounding data to assess the impact of varying environmental conditions on the spatial patterns of rainfall frequency and intensity in orographic precipitation in the Portland, Oregon, region of the U.S. Pacific Northwest (Fig. 1). Previous studies have shown the strong causal relationship between the geographic spatial distribution of orographic precipitation and wind direction (e.g., Frei and Schär 1998; Houze et al. 2001; Ralph et al. 2003; JH2005; Zängl 2008; PG2010). We build on this result by focusing our analysis of stability, cross-barrier wind speed, and

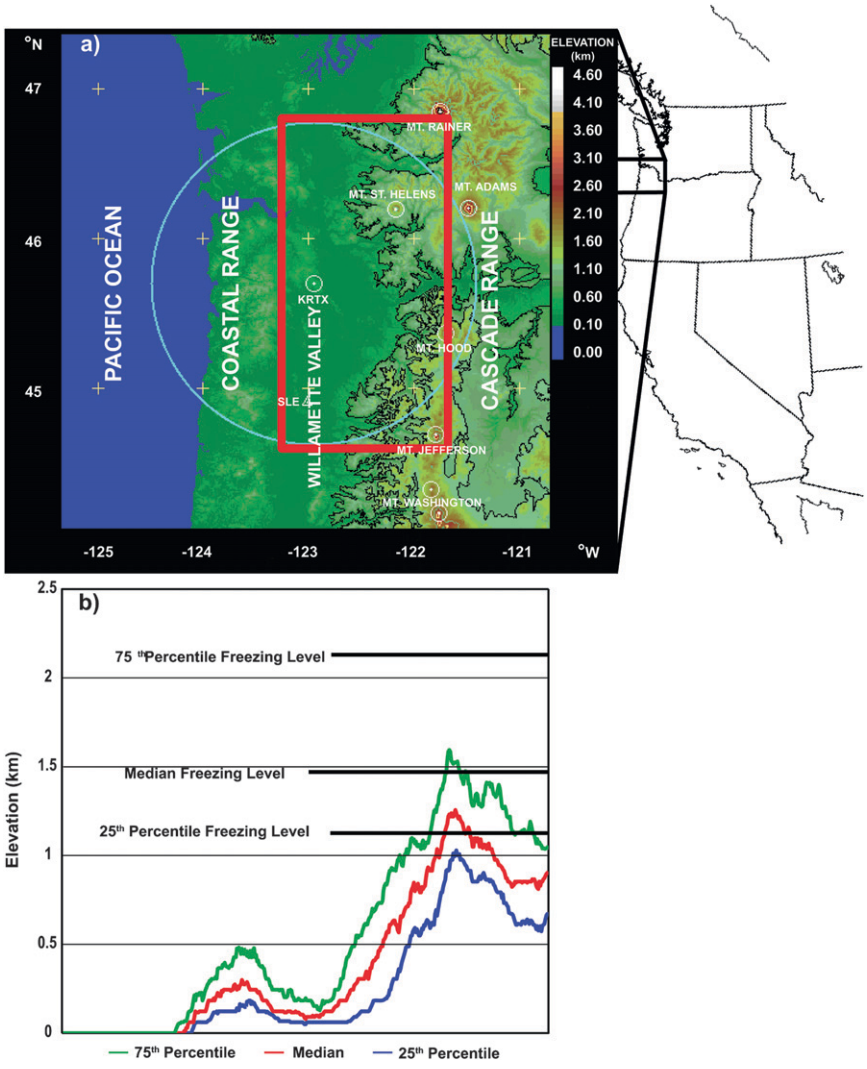

FIG. 1. (a) Topography of Portland, Oregon, and its surrounding areas (elevation in km MSL). Locations are labeled for the Pacific Ocean, Coastal and Cascade Ranges, Portland WSR-88D radar (KRTX) with 120-km range ring, Salem sounding (SLE), and Willamette Valley. The red box indicates Cascade windward slope region. (b) 25th, 50th, and 75th percentile east–west elevations for region 44.0°–47.3°N and 125.0°–120.75°W and storm 0°C level 25th, median, and 75th percentile heights from SLE.

0°C level height impacts on a subset of cases within the narrow mode in wind direction occurrence in the Portland storms (Fig. 2).

In a rough analogy to a model-sensitivity study, we utilize our large-storm database to construct composites of subsets of storms to isolate differences among the storm characteristics for similar wind direction and typical (between 25th and 75th percentiles), less than 25th percentile, and greater than 75th percentile categories of stability, cross-barrier wind speed, and 0°C level height. We focus on three characteristics of the reflectivity field: 1) where it rains, 2) the frequency of rainfall (i.e., how frequently it rains above a threshold rate), and 3) the relative intensity of rainfall. This methodology allows us to address several questions for Portland winter storms that cannot be addressed with the smaller sample size of multiweek field studies:

- What is the natural variability of storm environment characteristics in the Portland region?
  - — Are the distributions approximately Gaussian and well represented by mean values or not?
  - — What is the joint variability of key environmental variables?
  - — Where do the cases from IMPROVE II fit into the larger context?

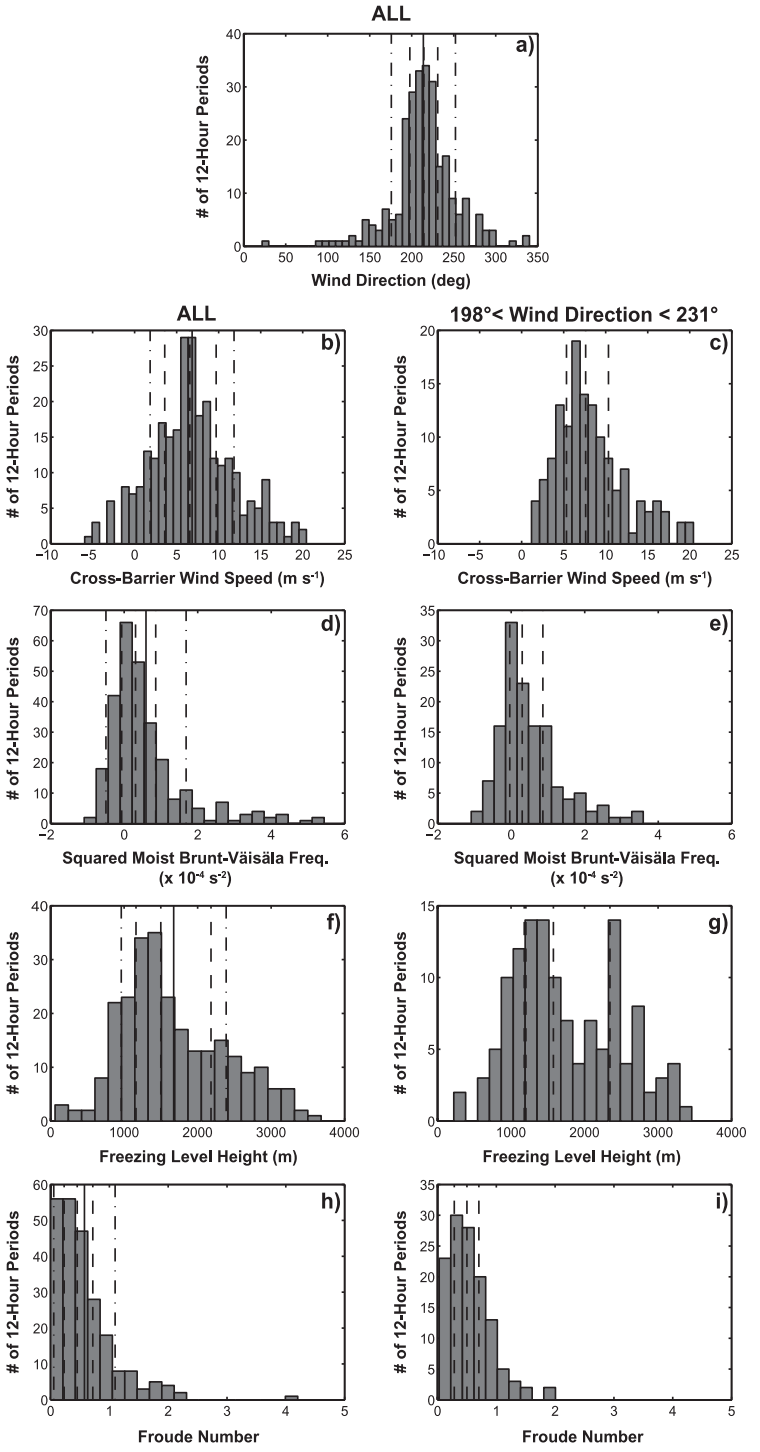

FIG. 2. Distributions of layer-average environmental characteristics based on Salem, Oregon, upper-air soundings for storm 12-h periods. (a) Distribution of wind direction for all 12-h periods. For other variables, distributions for (left) all periods are contrasted with (right) subset of 12-h periods with 198° ≤ wind direction ≤ 231°. (b),(c) Cross-barrier wind speed (m s^{-1}); (d),(e) squared moist Brunt-Väisälä frequency ($\times 10^{-4}$ s^{-2}); (f),(g) 0°C level height (m); (h),(i) Froude number. Solid lines in left column are the mean, and dash–dot lines in left column are ±1 std dev. Dash lines in all panels are 25th, 50th, and 75th percentiles.

- How do the three-dimensional (3D) spatial patterns of precipitation intensity and frequency change for different environmental characteristics?
- Which environmental variables have the largest impact on increasing frequency and intensity of precipitation?

Some background on Portland, Oregon, regional storm characteristics is provided in section 2. Section 3 describes our datasets and methods. Section 4 describes the observed distributions of environmental variables. Section 5 illustrates the sensitivity of the precipitation patterns to wind direction. Section 6 discusses typical storm characteristics, and section 7 describes the sensitivity of precipitation patterns to airflow characteristics. Section 8 addresses the broader impacts of the results and their relation to conceptual models and recent modeling studies. Conclusions are presented in Section 9.

2. Regional storm characteristics

Landfalling, extratropical, baroclinic waves, originating over the Pacific Ocean yield frequent rainfall during the cool season along the mountainous U.S. west coast. The more intense precipitation events are related to ''atmospheric rivers'' (Zhu and Newell 1998), narrow plumes of moisture associated with fronts on oceanic cyclones (Bao et al. 2006). These enhanced bands of vertically integrated water vapor typically form as the result of local moisture convergence (Bao et al. 2006). Under a subset of environmental conditions, the moisture can be traced back from the U.S. west coast to the tropics (Bao et al. 2006). These concentrated fluxes of water vapor produce heavy orographic precipitation events along mountain slopes (White et al. 2003; Ralph et al. 2004, 2005; Neiman et al. 2004, 2008), which can result in flooding and mudslides (e.g., White et al. 2003, Ralph et al. 2005; Galewsky and Sobel 2005; Reeves and Lin 2008). In the U.S. Pacific Northwest, atmospheric rivers are locally referred to as the ''Pineapple Express'' (Lackmann and Gyakum 1999; Colle and Mass 2000).

Portland, Oregon, (at 0.5 km MSL) is located at the intersection of the Columbia and Willamette Rivers within the broad Willamette Valley (Fig. 1). Separating Portland from the Pacific Ocean to the west is the Coastal Range, which has a mean crest level at 0.8–1 km MSL and is oriented in a north–south direction. To the east of Portland is the Cascade Mountain Range, which has typical crest levels ranging from 1.5–3 km MSL and is also oriented north–south. Over 2.5 m of rainfall occurs annually over the high peaks of the Coastal and Cascade Ranges in the Pacific Northwest (Daly et al. 1994). The majority of annual precipitation occurs during the winter season (Cayan and Roads 1984; Guirguis and Avissar 2008). Daily rainfall accumulations of 0.25 mm or more usually occur in Portland on more than half of the days from November through March [National Climatic Data Center (NCDC)]. In winter, cold easterly winds flowing through the Columbia Gorge can yield freezing rain in the city of Portland (Sharp and Mass 2004). Freezing rain does not impact our analysis because it has the same reflectivity properties as rain.

Cool-season storms are defined here as the set of heavy precipitation events occurring from 1 November through 15 April (with a few exceptions occurring a few days before or after).

3. Data and methods

We used operational datasets from the Portland, Oregon, region because this region has a good combination of frequency of precipitation events, radar coverage of windward slope precipitation, and close proximity of an upper-air sounding site to upslope flow and the operational radar site itself.

Surface observations of precipitation accumulation were not available for the windward slope to compare to the 12-h airflow characteristics and radar-derived statistics. The precipitation-gauge data that are available through the NCDC archives are hourly gauges located in the Willamette and Columbia River Valleys, which are not representative of upslope orographic flow, and gauges along the windward slope that do not report rainfall accumulations on time scales shorter than 24-h periods.

a. Radar data

National Weather Service (NWS) Level II Next Generation Weather Radar (NEXRAD) Weather Surveillance Radar-1988 Doppler (WSR-88D) radar observations for the Portland, Oregon, radar (KRTX; height = 0.479 km) were obtained from the NCDC. We used data for 117 winter-season storms (1 November–31 March) from 2003–06, which encompassed 2205 h total and comprised 261 12-h periods (Table 1). For comparison purposes, we also examined the eight IMPROVE II storm events (22 12-h periods; Table 1) from December 2001 analyzed in Medina et al. (2007). Table 2 places the Portland seasonal precipitation accumulations for 2003–06 into a 10-yr context and indicates the respective phases of the El Niño–Southern Oscillation (ENSO) and the Pacific decadal oscillation (PDO). There is substantial year-to-year variability in precipitation between 2000 and 2009, with the winter season of 2004/05 representing dryer conditions and the winter season of 2005/06 representing wetter conditions. The three winter seasons examined in this study do not include an ENSO cool phase event (La Niña) and the ENSO warm phase event (El Niño) in winter 2004/05 is weak. It is generally agreed that the

TABLE 1. Sample size of storm 12-h periods for different winter seasons examined in this study.

Time period	No. of 12-h periods
Total	283
IMPROVE II (26 Nov–22 Dec 2001)	22
Winter 2003/04	85
Winter 2004/05	56
Winter 2005/06	120

TABLE 2. Winter-season precipitation accumulation (1 Nov–31 Mar, at Portland, Oregon, airport, PDX) and ENSO and PDO phases for 2000–09 (http://cses.washington.edu/cig/pnwc/compensopdo.shtml). Oceanic Niño index (ONI, v3b) from the National Oceanic and Atmospheric Administration (NOAA)'s Climate Prediction Center Web site. PDO index from http://jisao.washington.edu/pdo/PDO.latest.

Time period	Total precipitation (cm)	ENSO phase	ONI index for DJF	PDO phase	PDO index for Jan
Winter 2000/01	29.97	Cool	−0.6	Cool	0.6
Winter 2001/02	67.77	Neutral	−0.1	Cool	0.27
Winter 2002/03	65.23	Warm	1.2	Warm	2.09
Winter 2003/04	55.58	Neutral	0.4	Warm	0.43
Winter 2004/05	33.78	Warm	0.7	Warm	0.44
Winter 2005/06	72.47	Neutral	−0.7	Cool	1.03
Winter 2006/07	68.99	Warm	0.8	Cool	0.01
Winter 2007/08	56.97	Cool	−1.4	Cool	−1.00
Winter 2008/09	42.91	Neutral	−0.8	Cool	−1.40

Pacific Northwest cool season is warmer and dryer than normal when the ENSO or PDO is in the warm phase and cooler and wetter than normal when the ENSO or PDO is in the cool phase (Hamlet and Lettenmaier 2007). The exact magnitudes of the precipitation anomalies depend on the years studied but are usually less than 10% (Castello and Shelton 2004; Hamlet and Lettenmaier 2007). The relative phasing of ENSO and PDO appear to have varying effects on precipitation accumulation as a function of time, with higher monthly accumulations when the two are in phase (Hamlet and Lettenmaier 2007) and higher daily accumulations when they are out of phase (Praskievicz and Chang 2009). Our 3-yr, 117-storm dataset is not fully representative of the long-term climatology but is sufficiently large and diverse to examine the sensitivity of precipitation patterns to different environmental conditions.

This study followed the general methodology of JH2005 for identifying heavy rain events. Storm days were selected based on daily rainfall totals of at least 5 mm from the Portland, Oregon, airport. Surrounding days that accumulated at least 2.5 mm were also examined along with the primary storm event. All the radar volumes obtained during the storm periods were analyzed. The initial storm-day definition was refined by examining KRTX radar data to determine the start and end times of radar echo within the radar domain to the nearest hour using the MountainZebra display (James et al. 2000). MountainZebra provides visualizations of radar images in horizontal and vertical cross sections with a detailed terrain field. The WSR-88D Level II data were converted to Universal Format (Barnes 1980), and quality control was applied to reduce nonmeteorological echo such as ground clutter and anomalous propagation. NWS clutter removal caused some data holes in the Level II data that were nonrecoverable. Data were then processed to dealias radial velocities (James and Houze 2001) and interpolated to 3D Cartesian grids utilizing the National Center for Atmospheric Research (NCAR) Earth Observing Laboratory's REORDER software using Cressman weighting (radius of influence settings: azimuth radius = 1.1° and z radius = 1 km). The interpolation grid was 120 km × 120 km × 16 km with 2-km spatial resolution in the horizontal and 1-km resolution in the vertical. Finally, the data were converted into Unidata's Network Common Data Format (NetCDF) for display in MountainZebra and statistical analysis in Matlab.

An important difference between our radar data processing and that of JH2005 is that JH2005 applied inverse range-squared smoothing with a 16-km horizontal radius of influence on their horizontal cross sections and a 6-km radius of influence smoothing on their vertical cross sections. We did not apply any smoothing to the output of the Cartesian interpolation step so as to preserve the signal of small-scale orographic enhancement. Additionally, we used all the available radar volumes (typically every six minutes) as compared to volumes obtained at one-hour intervals as was done in the multiseasonal studies of Houze et al. (2001) and JH2005.

Our study focuses on a portion of the Cascade windward slope (46.79°–44.6°N, 123.36°–121.66°W) rather than the entire radar domain. The radar beam from the Portland radar experiences considerable blockage over the coastal range (Westrick et al. 1999) to the point that the data are not adequate for the purposes of this paper. For this study, the most important limitation of the operational radar data is the coarse vertical resolution that is a consequence of the NWS precipitation-mode scan strategies. The study region overlaps with the northern portion of the IMPROVE II area but unfortunately does not extend to the central Oregon Cascade region, where high vertical resolution S-band profiler data were obtained during that project (Stoelinga et al. 2003; Medina et al. 2005, 2007).

b. *Upper-air sounding data*

The Salem, Oregon, upper-air sounding (SLE) site is 75 km south of KRTX in the Willamette Valley (Fig. 1). This location is just upwind of the Cascades and provides

TABLE 3. Environment and storm volume statistics for three winter storm sample plus IMPROVE II storms. Environmental characteristics are based on Salem, Oregon, sounding. Storm volume characteristics are derived from 3D radar data within the red box over the Cascade windward slope (Fig. 1).

	25th	50th	75th	90th	95th	Mean	Std dev
All 12-h periods							
WDIR (° azimuth)	198	214	231	258	279	214	38
U (m s^{-1})	3.5	6.5	9.6	14.0	15.7	6.7	4.9
N_m^2 ($\times 10^{-4}$ s^{-2})	−0.0434	0.329	0.904	2.057	3.383	0.631	1.120
Freezing-level height (m)	1162	1499	2182	2722	3030	1675	713
Fr	0.23	0.45	0.72	1.22	1.67	0.58	0.52
$Z \geq 13$ storm volume (km^3 hr^{-1})	1.6×10^5	3.4×10^5	6.5×10^5	9.3×10^5	13.2×10^5	4.5×10^5	4.0×10^5
$Z \geq 25$ storm volume (km^3 hr^{-1})	0.07×10^5	0.32×10^5	0.88×10^5	1.8×10^5	2.6×10^5	6.8×10^5	9.4×10^5
Subset of 2003–06 winter 12-h periods with 198° < WDIR < 231°							
U (m s^{-1})	5.3	7.6	10.0	14.6	16.3	—	—
N_m^2 ($\times 10^{-4}$ s^{-2})	−0.0386	0.305	0.885	1.823	2.508	—	—
Freezing-level height (m)	1191	1576	2345	2799	3039	—	—
Fr	0.29	0.50	0.70	1.01	1.29	—	—
Z13 storm volume (km^3 hr^{-1})	1.8×10^5	3.7×10^5	6.9×10^5	10.7×10^5	14.7×10^5	5.0×10^5	4.4×10^5
Z25 storm volume (km^3 hr^{-1})	0.08×10^5	0.34×10^5	1.1×10^5	2.2×10^5	3.1×10^5	0.77×10^5	1.1×10^5

a useful measure of the environmental characteristics. The Salem sounding is minimally influenced by winds through the Columbia Gorge (Sharp and Mass 2004).

Soundings were examined for the same time periods as the KRTX WSR-88D data to obtain upwind flow characteristics related to Cascade Range orographic enhancement. Layer averages of upper-air sounding data were computed from 1010–770 hPa, which corresponds to the altitude of the SLE station at 0.061 km MSL to approximately 2.2 km MSL. To characterize stability, we use the 1010–770-hPa layer-averaged [Reinecke and Durran (2008), their Eq. (1)] squared moist Brunt–Väisälä frequency [N_m^2; Durran and Klemp 1982; their Eq. (5)]. We assumed that the air was saturated [relative humidity (RH) = 100%] in the calculation of N_m^2. Using the 800–900-hPa-layer average similar to JH2005, the Fr was calculated from the Salem, Oregon, soundings using

$$\mathrm{Fr} = \frac{U}{N_m h}, \tag{2}$$

where h is the average crest height of the Cascades (1.8 km), U is the cross-barrier wind speed in m s^{-1}, and N_m is the moist Brunt–Väisälä frequency. Following previous studies of storms in this geographic region, we approximate the cross-barrier wind as the wind component from the 270° azimuth, which is roughly perpendicular to the Cascade Range. Although we approximate the cross-barrier flow as two-dimensional, the actual flow along a local slope is subject to the entire range of natural topographic scales, the smaller of which are without question 3D.

In this paper, we use "freezing-level height" and "0°C level height" interchangeably. Rain-layer depth plus melting-layer thickness is equal to the 0°C level height (Battan 1973). Neither the upper-air soundings nor operational radar data provide a good measure of melting-layer thickness, but it is typically a few 100 m in this region (Yuter et al. 2006; Medina et al. 2007) and varies within and among storms.

The storms during the 2003–06 cool seasons were subdivided into 261 12-h periods that are ±6 h from the upper-air sounding times of 0000 and 1200 UTC. The data were grouped into subsets by wind direction, cross-barrier wind speed, stability, and 0°C level height (Table 3). For convenience, we will refer to the set of radar volumes with echo anywhere in the Portland, Oregon, radar domain within the 12-h period as the "12-hour storm volume set." If the storm does not persist for the entire 12-h period, we used only the portion of that period with radar echo. Just less than half (47%) of the 12-h periods had radar echo for the entire 12 h. The use of the profile at Salem to represent the environment over the entire radar domain ±6 h from the sounding time has limitations because variables may have sharp gradients across frontal boundaries within the domain, and the storm structures will move and evolve during the 12-h period. Model reanalysis products such as the National Centers for Environmental Prediction (NCEP)–NCAR reanalysis (Kalnay et al. 1996) are currently available four-times daily. For the purposes of this paper, the advantages in accuracy of the observed twice-daily upper-air soundings outweigh the more frequent but more uncertain reanalysis. Although wind profiles from NWS velocity–azimuth display (VAD) products are available when sufficient echo is present around the KTRX radar, they do not have accompanying thermodynamic data. Thus, VADs were not used in this study.

c. Definitions of storm statistics

There is a substantial body of literature detailing the uncertainties in estimating surface precipitation from radar reflectivity data (e.g., Austin 1987; Joss et al. 1998; Krajewski and Smith 2002; Yuter 2002; Tanré et al. 2008). Among the potential sources of error most relevant to the Portland, Oregon, region winter storms are changes in the vertical profile of precipitation from the height of the radar beam to the surface and signal enhancement by melting particles. These issues complicate the production of high-quality surface precipitation maps from radar data.

As fronts cross the Pacific Northwest, the altitude of the 0°C level and the associated melting band can change by more than 1.5 km for a single storm (Medina et al. 2007). The application of a reflectivity–rain rate (Z–R) relation for rain mapping is hindered when the melting layer is at low levels (Yuter 2002). The brightband reflectivity, which represents the backscatter from a mixture of rain and partially melted ice, can be mistaken for rain, thus yielding incorrect values of rainfall. Use of storm-average radar reflectivity can potentially confuse the presence of a bright band with localized orographic enhancement. This was a weakness of several previous analyses of 3D radar data (Houze et al. 2001; JH2005; Medina et al. 2007). To mitigate these problems, we use exceedance thresholds of $Z \geq 13$ dBZ, and $Z \geq 25$ dBZ to characterize precipitation frequency. Use of the 13-dBZ threshold allows us to account for the frequency of precipitation echo in a manner that is relatively insensitive to the absence or presence of the radar bright band. JH2005 also used a 13-dBZ threshold to determine the frequency of precipitation within their study area. The 13-dBZ threshold corresponds to a rain rate of ~0.2 mm h^{-1} and 25 dBZ corresponds to ~1.3 mm h^{-1} (Hagen and Yuter 2003). The frequency was computed by summing radar pixels greater than or equal to the threshold dBZ within the 3D radar volumes for groups of 12-h storm volume sets, dividing by the number of volumes and multiplying by 100 to obtain a percentage.

Hydrological applications use rainfall accumulations that are a function of both rainfall rate and duration [Eq. (1)]. Exceedance frequencies address duration. Since the typical rain-rate distribution is closer to a lognormal distribution than a Gaussian distribution (Hagen and Yuter 2003), linear average rain rates are very sensitive to outlier extreme rain rates and are often unrepresentative of the rain-rate median and distribution mode. We use the ratio of exceedance frequencies for $Z \geq 25$ dBZ over the frequency of $Z \geq 13$ dBZ as a measure of precipitation intensity because high-quality quantitative rain rates are not available for this dataset.

Storm precipitation echo volume per hour is defined here as a metric of storm scale. Storm precipitation echo volume is computed by summing the 3D volume of radar reflectivity pixels ≥ 13 dBZ and ≥ 25 dBZ for radar volumes within the 12-h storm volume set and dividing by the number of hours with echo.

Grid points within the accumulated 3D volumes with small sample sizes, defined here as having a frequency of radar echo with $Z \geq 13$ dBZ of less than 20%, are set to missing in the horizontal and vertical cross-section plots. Removed areas include regions that experience beam blocking by terrain and higher altitudes in the volume scan that have infrequent echo. Horizontal cross sections of the interpolated 3D radar volumes are shown at 2-km altitude, which has good regional coverage by the Portland WSR-88D, to characterize flow over the western, windward slope of the Cascades.

We use medians and percentiles rather than means and standard deviations because the distributions of most of the variables of interest are not Gaussian (Figs. 2 and 3). Taleb (2007) presents a compelling case on the importance of outliers and the problems of using means to represent non-Gaussian distributions. Use of percentiles rather than means improves the reproducibility of our results in the sense of repeating the calculations with an independent dataset of cool-season storms for the same region.

4. Distributions of environmental variables

Histograms of layer-averaged wind direction, cross-barrier wind speed N_m^2, 0°C level height, and Fr illustrate the distribution of environmental conditions for 12-h storm periods over the three cool seasons (Figs. 2a, 2b, 2d, 2f, and 2h). Values for means, standard deviations, quartiles, and the 90th and 95th percentiles are given in Table 3 for the full set of storms. Storm and environment characteristics are also provided in Table 3 for the subset of storm periods with wind direction between 198°–231° azimuth, which represent the 25th–75th percentiles for wind direction. For the wind direction 198°–231° azimuth subset (Figs. 2c, 2e, 2g, and 2i), the distributions are far from Gaussian. Cross-barrier wind speed N_m^2 and Fr are skewed toward lower values, and 0°C level height is bimodal (Figs. 2c, 2e, 2g, and 2i). The distribution of storm precipitation echo volume per hour for $Z \geq 25$ dBZ is more strongly skewed toward smaller values than the corresponding distribution for $Z \geq 13$ dBZ for all storms and the subset of storms with winds from 198°–231° azimuth (Fig. 3).

Figure 4b is similar to Fig. 3 from JH2005 and shows layer-averaged (1010–770 hPa) wind direction versus N_m^2. JH2005 found that most storms in the Eureka, California, region, which is 600 km to the south of Portland, Oregon, had N_m^2 between $\pm 1 \times 10^{-4}$ s^{-2}, indicating small deviations from moist neutral conditions. PG2010 observed N_m^2 values between -1.5×10^{-4} and 1.8×10^{-4} s^{-2} for

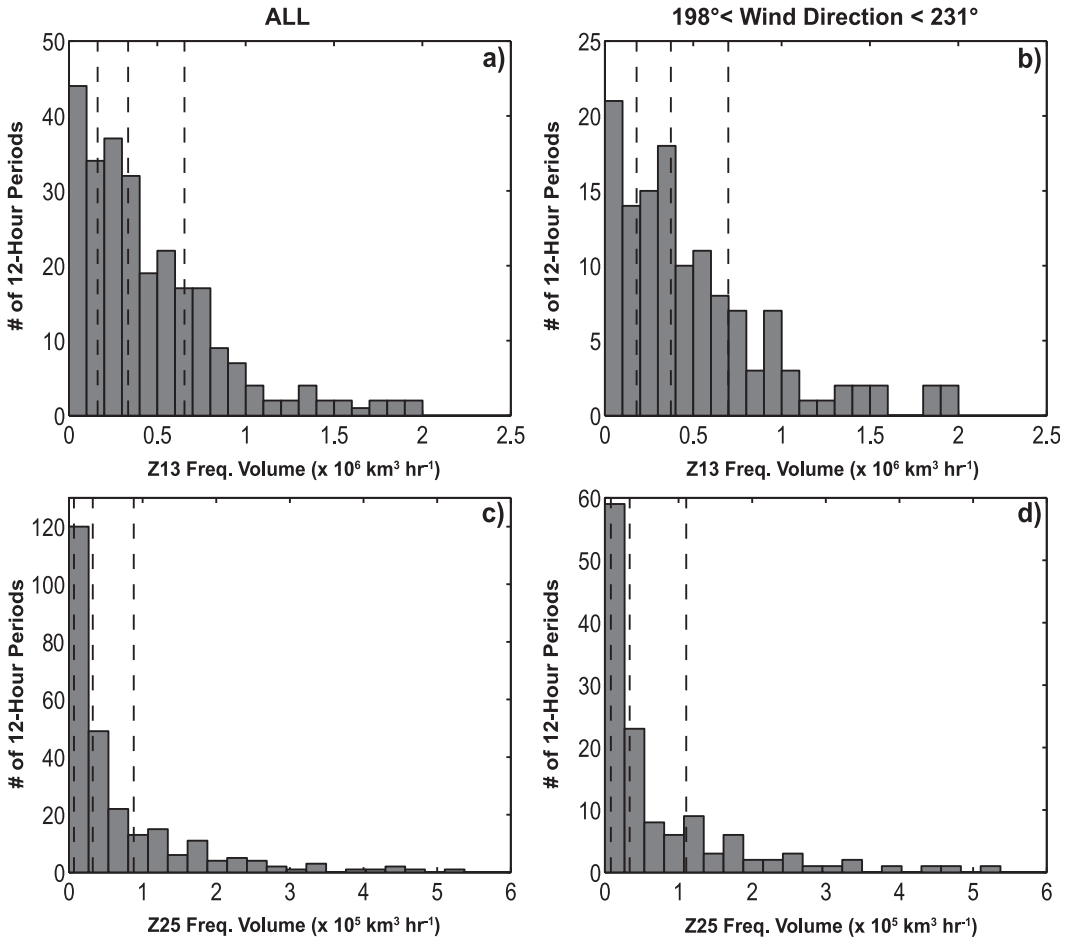

FIG. 3. Storm precipitation echo volume per hour over Cascade windward slope box boundaries defined in text. For all storm periods: (a) $Z \geq 13$ dBZ ($\times 10^6$ km^3 h^{-1}) and (c) $Z \geq 25$ dBZ ($\times 10^5$ km^3 h^{-1}). For subset of storm periods for wind directions between 198°–231°: (b) $Z \geq 13$ dBZ and (d) $Z \geq 25$ dBZ. Dashed lines are 25th, 50th, and 75th percentiles.

widespread precipitating storms over all seasons in the Southern Alps. During MAP, the intensive observation period (IOP) 2b unstable case had layer-average N_m^2 of approximately -0.4×10^{-4} s^{-2}, and the IOP8 stable case had a value of approximately 1.6×10^{-4} s^{-2} (Medina and Houze 2003). In comparison, the distribution of N_m^2 in the Portland area is skewed toward near neutral conditions and includes some samples with strong stability ($N_m^2 > 2 \times 10^{-4}$ s^{-2}; Figs. 2 and 4; Table 3). The stable environment is the result of land-falling baroclinic systems (not shown), which are stably stratified at low levels. Based on the Fr criteria, the majority of Portland area winter storms are associated with at least partial flow blocking below midmountain level (Fr < 1; Figs. 2 and 4g–4i). Flow at the lowest levels (0.061 to 1.11 km MSL; not shown) tends to be more southerly than the layer-average flow between 0.061 and 2.2 km MSL.

The scatterplots of N_m^2 versus freezing-level height (Fig. 4e) and cross-barrier wind speed versus freezing-level height (Fig. 4f) indicate that the largest storm volumes per hour (>90th percentile) are most frequently associated with a combination of deeper rain layer (higher 0°C level), strong cross-barrier wind speed, and neutral to slightly stable conditions. The cross-barrier wind speed versus 0°C level height scatterplot also indicates that these variables are essentially independent for this dataset (Fig. 4f).

IMPROVE II took place from 26 November to 22 December 2001 and obtained data from storms over 17 IOPs, some of which sampled different phases of the same storm (Stoelinga et al. 2003). It would be unlikely for a small sample over 4 weeks to have a distribution representative of 117 storms over three winters. The IMPROVE II IOPs sampled a wide range of cross-barrier wind speeds for 0°C level heights near 1-km altitude but included only a few samples with 0°C level height higher than 1.5-km altitude. More of the IMPROVE II storm periods had wind directions outside the 25th to 75th percentiles than inside, thus yielding an unrepresentative sample for wind direction.

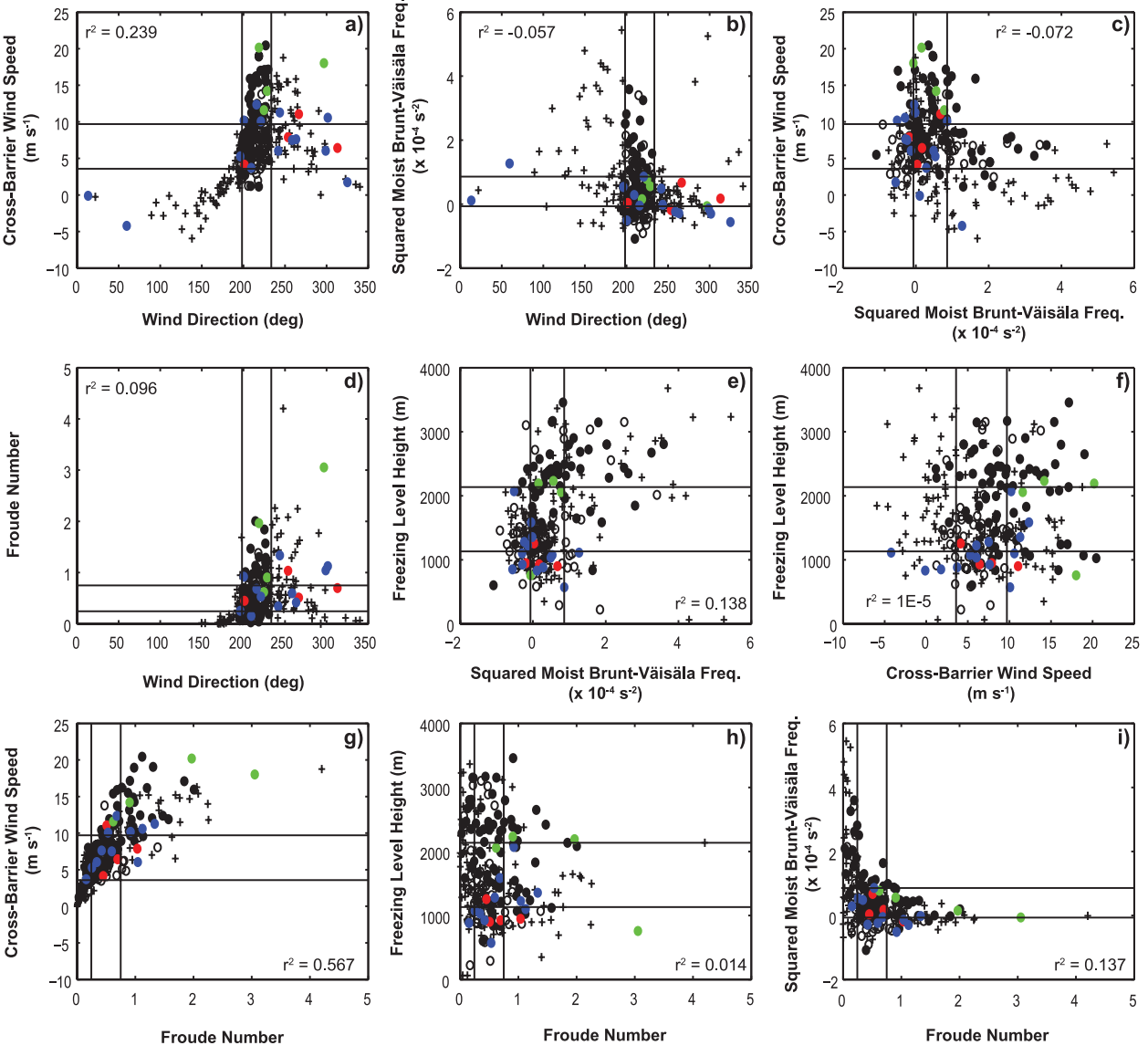

FIG. 4. Scatterplots of environmental variables. (a) Wind direction (°) vs cross-barrier wind speed (m s^{-1}); (b) wind direction vs squared moist Brunt–Väisälä frequency (N_m^2; $\times 10^{-4}$ s^{-2}); (c) N_m^2 vs cross-barrier wind speed; (d) wind direction vs Fr; (e) N_m^2 vs 0°C level height (m); (f) cross-barrier wind speed vs 0°C level height; (g) Fr vs cross-barrier wind speed; (h) Fr vs 0°C level height; and (i) Fr vs N_m^2. Color coding of symbols are black = 2003–06 storm subset; green = 13–14 Dec 2001 IMPROVE II case; red = 3–4 Dec 2001 IMPROVE II case; and blue = other IMPROVE II cases. Symbol shape coding is + = cases that do not have wind direction between 198°–231° azimuth; ○ = wind direction between 198°–231° azimuth and $Z \geq$ 25-dBZ storm volume < 90th percentile; and ● = wind direction between 198°–231° azimuth and $Z \geq$ 25-dBZ storm volume > 90th percentile. Horizontal and vertical lines are 25th and 75th percentiles for the relevant variable. Coefficient of determination (r^2) is indicated in each panel.

The 13–14 December 2001 heavy rainfall IMPROVE II storm with 30 m s^{-1} crest-level flow (Garvert et al. 2007) is an outlier in terms of layer-average cross-barrier wind speed (20.2 m s^{-1}) and is stronger than 99% of the 12-h storm periods examined for the 2003–06 cool seasons (Figs. 4a, 4c, and 4g). Within the warm sector, the 13–14 December 2001 storm had 0°C level heights near the 75th percentile. The 3–4 December 2001 weak flow case examined in Colle et al. (2008) had more typical cross-barrier wind speeds and was near the 25th percentile in 0°C level height. During IMPROVE II, high 0°C levels > 75th percentile only occurred in conjunction with $U >$ 75th percentile, a limitation that did not permit investigation of high 0°C level heights and lower cross-barrier winds using the field project dataset.

The N_m^2 versus freezing-level height plot (Fig. 4e) shows a weak association for more stable conditions to occur

coincident with higher freezing levels. Strong stabilities $N_m^2 > 2 \times 10^{-4}$ s^{-2} only occurred for cross-barrier wind speeds < 10 m s^{-1} (Fig. 4c). For this storm dataset, there is little correlation between N_m^2 and wind direction (Fig. 4b).

Higher cross-barrier wind speed and higher freezing-level height have better correspondence to larger storm volume than variations in N_m^2 or Fr (Figs. 5 and 6). These associations are slightly stronger for storm precipitation echo volume per hour calculated for $Z \geq 25$ dBZ compared to $Z \geq 13$ dBZ. Most of the variation in Fr is a function of U rather than stability (Figs. 4g and 4i). Previous orographic storm climatologies (JH2005; PG2010) did not directly address the relative contributions of variation in U versus N_m^2 to Fr. Dominance of U over N_m^2 is likely in regions where the natural variations in N_m^2 are small.

5. Wind direction composites

Consistent with the results of previous studies for other geographic regions (e.g., Frei and Schär 1998; Houze et al. 2001; JH2005; PG2010; Ralph et al. 2003; Zängl 2008), the spatial distribution of orographic precipitation over the Cascades is highly dependent on wind direction (Fig. 7). Winds typically veer with height between near the surface and 4-km altitude, which is indicative of warm advection (not shown) and orographic deflection, with the greatest directional shear occurring in south-southwest storms (not shown).

Local maxima in exceedance frequency and intensity do not typically occur on drainage divides in this region. The highest values in exceedance frequency over both the Cascade and Coastal Mountains occur in the 198°–231° azimuth subset (Fig. 7e) within the Lewis River drainage basin. The strong flow (peak radial velocities near the radar ~18 m s^{-1}) and veering of storms in the 198°–231° subset suggests that these events are associated with more robust baroclinic waves. In contrast, the <198° azimuth subset has the weakest cross-barrier winds (all samples are <25th percentile for U; peak radial velocities near the radar ~13 m s^{-1}) and weakest enhancement in exceedance frequency (Figs. 4a and 7). For wind directions >231°, cross-barrier winds speeds include a wide range of values, and exceedance frequencies are intermediate between those for the <198° and 198°–231° wind direction subsets. For wind directions >231°, the location of high precipitation frequencies along the Cascade lower slope is rotated clockwise (cf. Figs. 7e and 7h), consistent with the wind direction. The precipitation frequency values are smaller than the peak values in the Lewis River valley for the 198°–231° azimuth subset. The exceedance frequency plots in Fig. 7 also contain radar-concentric artifacts related to interpolation of the polar coordinate scan strategy to Cartesian coordinates. We focus on the Cascade windward slope between 30 and 100 km from the radar to minimize the influence of these artifacts on our results.

6. Characteristics of a typical storm

A typical storm in the Portland, Oregon, region is defined here as having joint characteristics within the 25th and 75th percentiles for wind direction, cross-barrier wind speed N_m^2, and 0°C level height. This definition yielded 18 12-h periods (Table 4), which were combined into a composite for a typical storm in Fig. 8. Mount St. Helens (peak elevation 2549 m) is located at the southwest end of the narrow wedge of radar beam blockage 81 km to the northwest of the radar location. Just to the southwest of Mount St. Helens, precipitation is preferentially enhanced over the Lewis River valley and its north ridge. Compared to the median radial velocity data at 2-km altitude (Fig. 8a), the upper-air sounding data indicate more southerly flow within the broad Willamette Valley for levels below 2-km altitude (not shown). Close examination of the terrain map relative to the locations of precipitation frequency maxima to the northeast, west, and southwest of the radar suggests that there is local up-valley flow for some of the smaller valleys along the Cascade windward slope.

To illustrate the vertical structures of flow and precipitation for comparison among different subsets of our dataset and to other studies, we show a vertical cross section (white line in Fig. 8) that is nearly parallel with the mesoscale low-level flow and not subject to beam blockage. The spatial pattern of precipitation enhancement within a vertical cross section through the 3D storm composite is highly sensitive to the exact position of the cross section chosen. Examination of many cross sections (not shown) indicated that enhancements in precipitation exceedance frequency are usually associated with local ridges or regions immediately upwind of ridges (e.g., Fig. 8).

The specific locations of precipitation enhancement can vary with the precipitation exceedance threshold used (e.g., compare $Z \geq 13$ dBZ versus $Z \geq 25$ dBZ frequencies in Figs. 8b and 8c). For example, in the Cascade foothills ~65 km east of the radar near Camas, Washington, along the Columbia River (Fig. 8), there is a local maximum in enhancement in the frequency of $Z \geq 13$ that is not present for $Z \geq 25$ dBZ. Along the vertical cross section, the pattern of enhancement over terrain for $Z \geq 13$ dBZ versus $Z \geq 25$ dBZ (Figs. 8e and 8f) is grossly similar but differs in detail (e.g., between 60- and 72-km distance along the cross section) and is not simply the same pattern at different magnitudes. Note that precipitation frequency for $Z \geq 5$ dBZ (Figs. 8h and 8j) has a qualitatively similar spatial pattern to precipitation frequency for $Z \geq 13$ dBZ, (Figs. 8b and 8e), though with different magnitudes. This similarity between the $Z \geq 5$ dBZ and $Z \geq 13$ dBZ

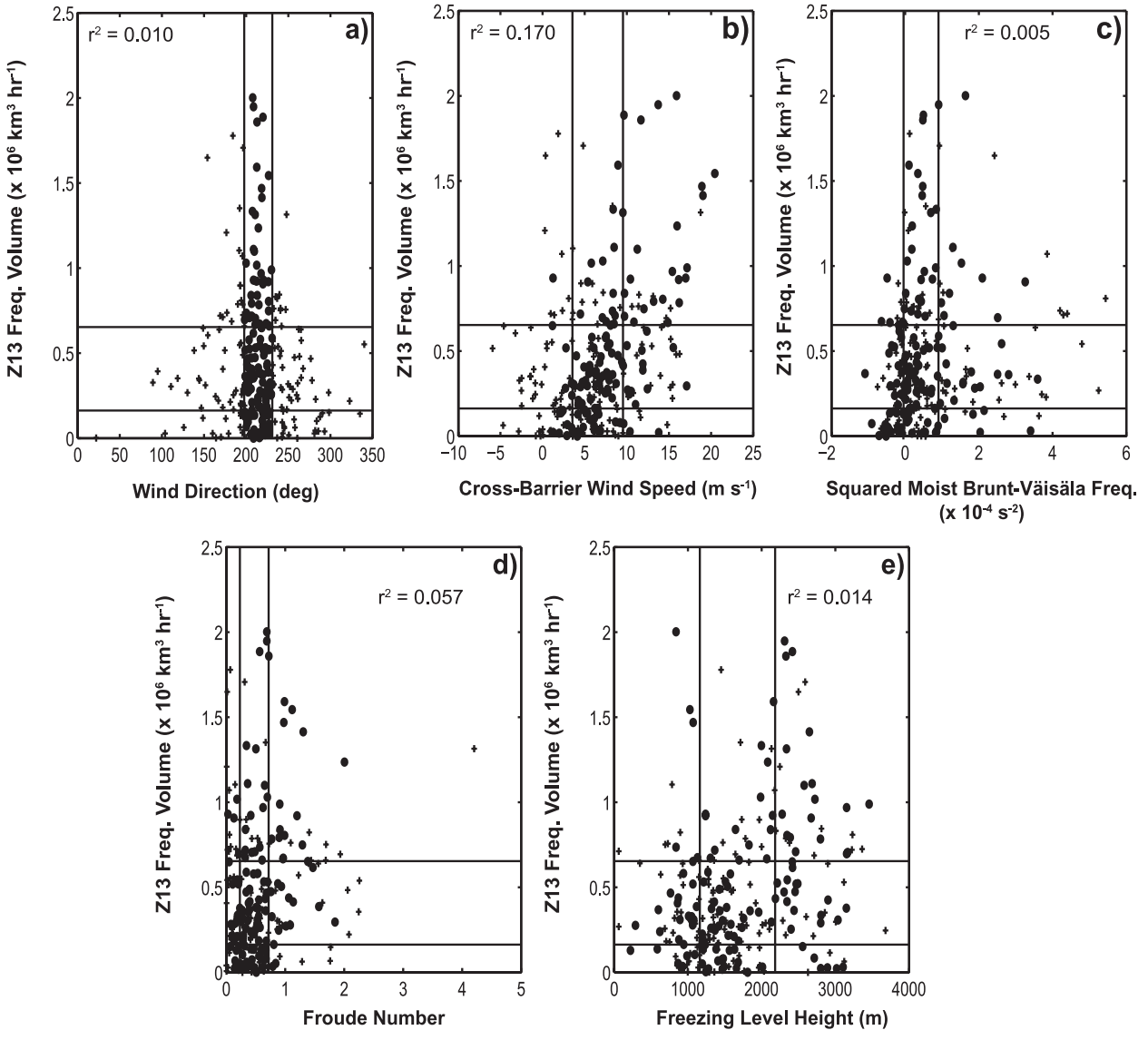

FIG. 5. Scatterplots of environmental variables vs $Z \geq 13$ dBZ ($\times 10^6$ km^3 h^{-1}) storm precipitation echo volume per hour. (a) Wind direction (°); (b) cross-barrier wind speed (m s^{-1}); (c) squared moist Brunt–Väisälä frequency ($\times 10^{-4}$ s^{-2}); (d) Froude number; and (e) 0°C level height (m). Symbols are coded as follows: + = cases that do not have wind direction between 198°–231° azimuth and ● = wind direction between 198°–231° azimuth. Horizontal and vertical lines are 25th and 75th percentiles for the relevant variable. Here, r^2 (coefficient of determination) is indicated in each panel.

exceedance thresholds indicates that use of a lower dBZ threshold than 13 dBZ does not significantly change the locations of precipitation frequency maxima. Brightband contamination would likely manifest as a concentric arc to the radar location (see Seo et al. 2000, their Fig. 4b), which is not present in these plots.

Examination of these and many other cross sections (not shown) indicated that the locations of enhanced frequency versus relatively heavier precipitation can overlap but often differ in detail and spatial extent. Near the Lewis River valley southwest of Mount St. Helens and in the Columbia River valley east of the radar, distinct differences in the detailed patterns of frequency versus intensity occur (Figs. 8b and 8g). The localized areas that experience more frequent precipitation echo ≥ 25 dBZ do not always intersect with areas with more frequent precipitation echo ≥ 13 dBZ as would be expected if precipitation rate were only a function of upslope vertical motions. Rather, the disjoint maxima of higher intensity versus frequency are an indication that heavier precipitation can be triggered outside of regions where lighter precipitation occurs most frequently. A likely agent is riming growth, which

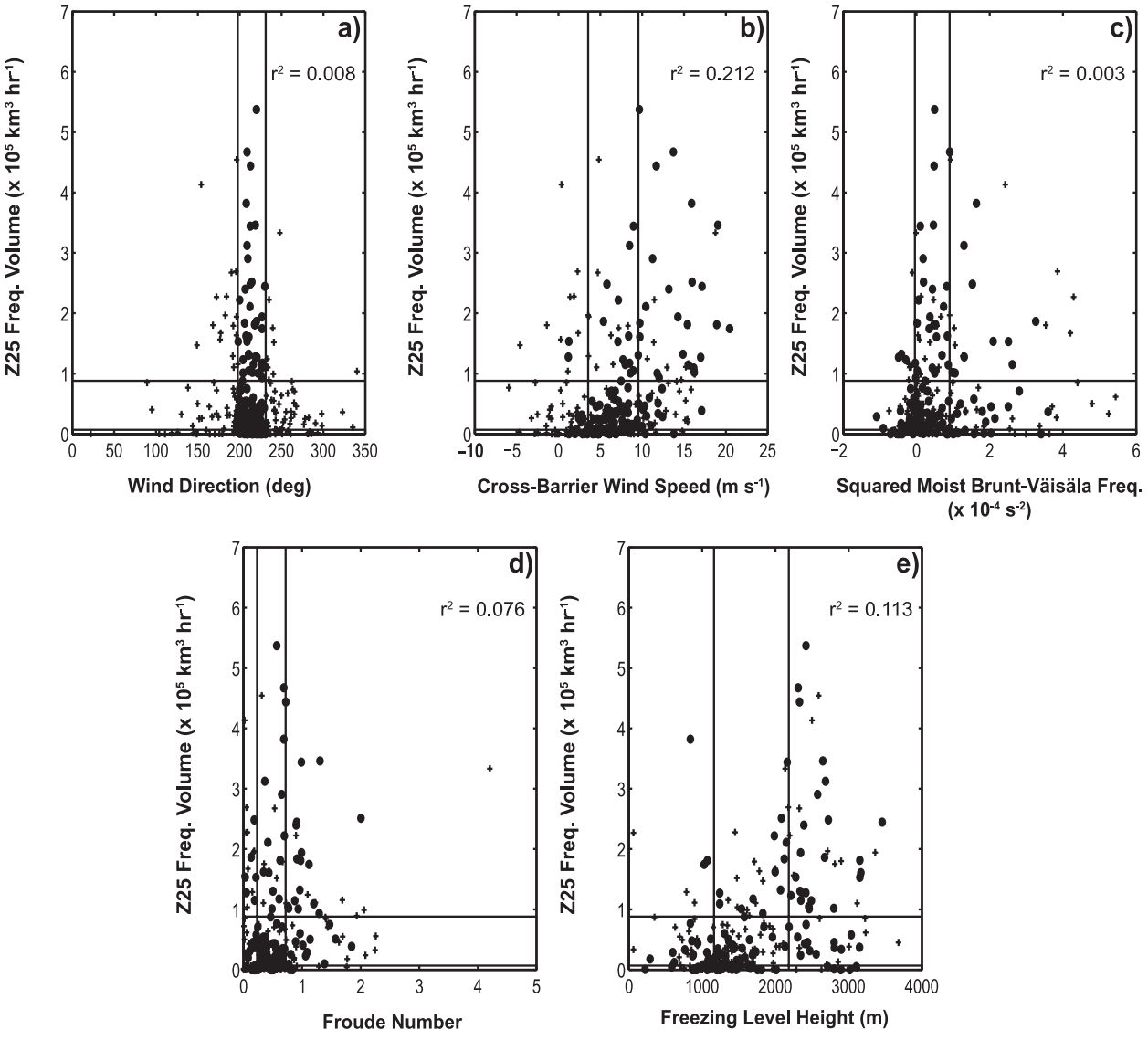

FIG. 6. As in Fig. 5, but for environmental variables vs $Z \geq 25$ dBZ ($\times 10^5$ km^3 h^{-1}) storm precipitation echo volume per hour.

is fastest where conditions favor riming of frozen drops (Braham 1964; Johnson 1987), such as a juxtaposition of strong upward motions below and just above the 0°C level. Localized strong updrafts could occur through a variety of processes, including strong winds over steep ridges and shear between distinct air layers flows (Houze and Medina 2005). In the Columbia River valley 50–75 km to the east of the radar, there are locations with $Z \geq 13$ dBZ frequency of 80% and $Z \geq 25$ dBZ frequency of 25% close by locations with $Z \geq 13$ frequency of 73% and $Z \geq 25$ frequency of 45%. Although we do not have surface precipitation intensities to determine the accumulations precisely, these nearby areas are approaching similar storm total accumulations from longer duration of lighter rain rates versus shorter durations of higher rain rates.

Given the sensitivity of the results to the Z threshold, it is likely that other thresholds will indicate different degrees of overlap between locations of enhancement in precipitation frequency versus intensity. This sensitivity needs to be kept in mind when comparing studies and interpreting results. JH2005 (their Fig. 6) found that the spatial patterns of precipitation frequency and intensity were qualitatively similar, but this finding is likely a result of their smoothing of the radar data.

7. Sensitivity of precipitation patterns to airflow characteristics

Figures 9, 10, and 11 illustrate the variations in the spatial pattern of precipitation frequency and intensity for

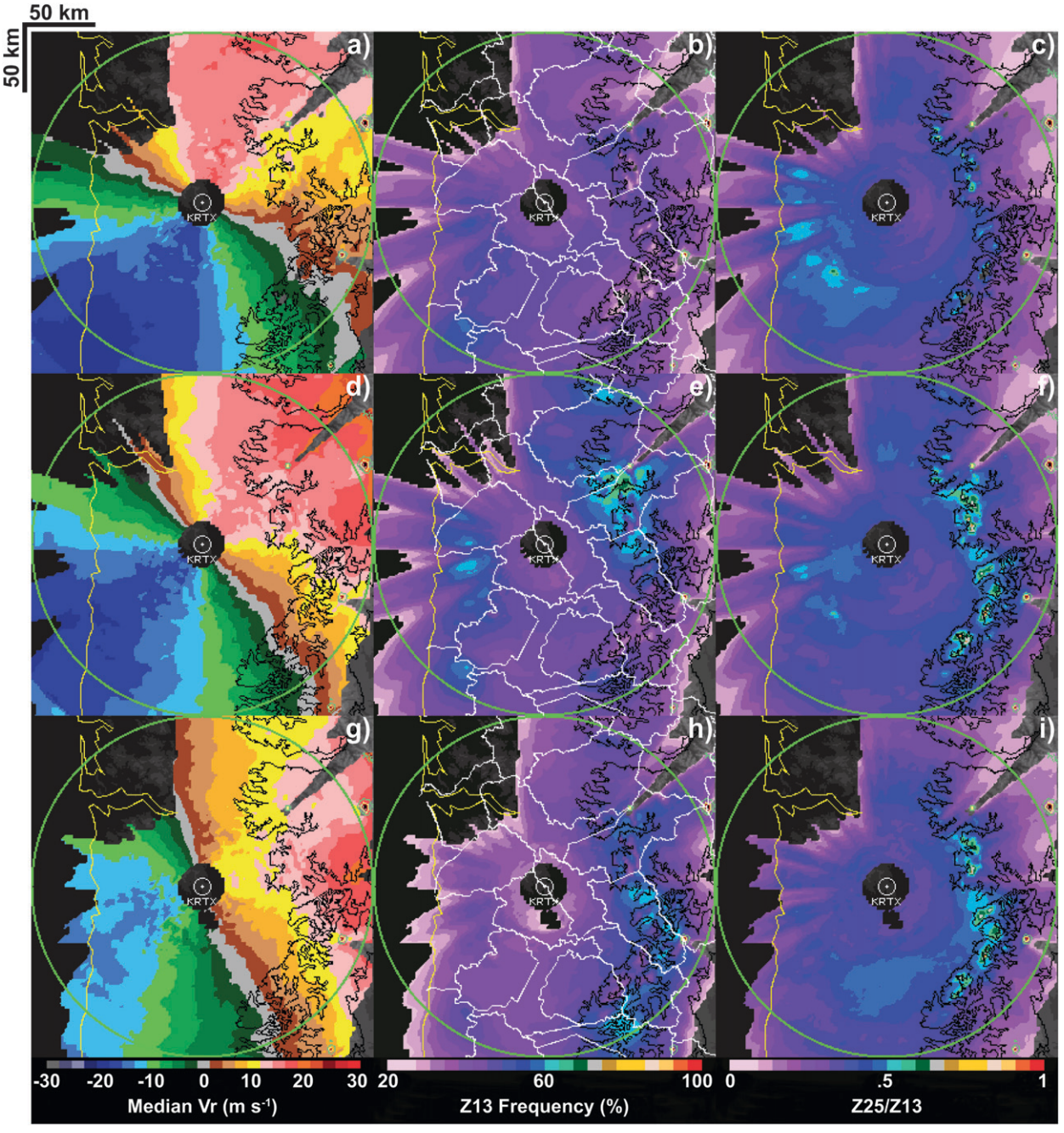

FIG. 7. Horizontal spatial patterns of radar-derived variables at 2-km altitude associated with different wind directions. (a)–(c) Wind direction $< 198°$; (d)–(f) wind direction between 198°–231° azimuth; and (g)–(i) wind direction $> 231°$. (a),(d),(g) Median radial velocity (Vr; m s^{-1}); (b),(e),(h) $Z \geq 13$ dBZ exceedance frequency (%) with watershed drainage divides overlaid (white lines); and (c),(f),(i) Z25/Z13 ratio (relative precipitation intensity). See Table 4 for sample sizes and median characteristics. [Watershed boundaries source: coordinated effort between the U.S. Department of Agriculture's Natural Resources Conservation Service (USDA NRCS), the U.S. Geological Survey (USGS), and the Environmental Protection Agency (EPA); http://datagateway.nrcs.usda.gov.]

different environmental conditions within the subset of storms with low-level wind directions between 198°–231° azimuth. Table 4 shows the sample size of 12-h periods and the median values for the environmental variables for the subplots shown in Figs. 9, 10, and 11. Among stability U and 0°C level height, the cross-barrier wind speed has the largest individual impact on the frequency of precipitation exceeding the $Z \geq 13$ dBZ threshold at a given

TABLE 4. Sample size of storm subset 12-h periods and corresponding median values of U, 0°C level height, and N_m^2 derived from Salem, Oregon, upper-air sounding.

Subset	No. of 12-h periods	U, median (m s^{-1})	Freezing-level height, median (m)	N_m^2, median ($\times 10^{-4}$ s^{-2})
<198° azimuth	67	1.6	1721	0.60
198°–231° azimuth	129	7.6	1576	0.30
>231° azimuth	65	8.7	1343	0.16
Typical: 198°–231° and (N_m^2, U, 0°C level height from 25%–75%)	18	7.8	1636	0.25
198°–231° and $N_m^2 < 25\%$	32	6.6	1312	−0.28
198°–231° and $N_m^2 > 75\%$	32	6.2	2330	1.57
198°–231° and $U < 25\%$	32	4.0	1438	0.12
198°–231° and $U > 75\%$	32	13.5	2109	0.44
198°–231° and 0°C level height < 25%	32	6.1	941	0.11
198°–231° and 0°C level height > 75%	32	8.6	2701	0.93
198°–231° and $U > 75\%$ and 0°C level height > 75%	11	13.8	2798	0.83

location, and stability has the smallest individual impact. The role of U in orographic precipitation enhancement is associated with two complementary physical processes. By simple geometry, flow over an upward-tilted slope has a larger magnitude vertical velocity component when the wind speed is higher. Linear orographic models (e.g., Smith and Barstad 2004) and models with more complex physics (e.g., Colle 2004) indicate strong sensitivity of precipitation to cross-barrier wind speed. Additionally, the interaction of winds of a given direction with topography can yield local convergence that preferentially directs preexisting cellular convection to a preferred location along a mountain barrier. Higher wind speeds will increase the flux of preexisting convective cells intersecting the slope (e.g., Fig. 12). Both increased vertical velocity along the windward slope and the increased flux of preexisting convective cells moving upslope contribute to enhanced orographic precipitation. Other factors such as increased cross-barrier moisture flux and potential instability also contribute to the high precipitation intensities associated with stronger cross-barrier wind speed.

The role of a deep rain layer (high 0°C level height) in the spatial pattern and intensity of precipitation over a windward slope has been previously recognized in several climatologies of U.S. west coast flooding events (Ralph et al. 2003; Lundquist et al. 2008; Neiman et al. 2008). However, the relative importance of rain-layer depth on the observed spatial pattern of precipitation over a large set of storms has not been previously examined in relation to U and N_m^2. The winter storms in the Portland, Oregon, region experience a wide range of 0°C level heights (Table 3), allowing us to explore this sensitivity. For the Cascades windward slope near Portland, the precipitation relative intensity (Z25/Z13 ratio) is slightly more sensitive to freezing-level height than U (Figs. 9 and 10). The largest areas of high relative intensities (>0.7) are observed for 0°C level heights > 75th percentile (Figs. 9i and 10i) corresponding to samples with 0°C levels > 2345-m altitude and median 0°C level height of 2701 m (Tables 3 and 4). There may be some radar brightband contamination contributing to the higher relative intensities, but the enhanced pattern in Fig. 9i is not concentric to the radar and roughly follows the 0.5-km altitude terrain contour to the east of the radar, indicating a primarily meteorological source.

Deep moist layers and high cross-barrier winds combine to yield high water vapor fluxes directly upwind of the barrier and high precipitation frequency and relative intensity over the barrier (Fig. 11). This joint subset is more frequently associated with larger storm echo volumes than other combinations of rain-layer depth and U (Fig. 4f). Examination of the cross section of median radial velocity in Fig. 11 shows strong vertical shear (radial velocity: 12.5 m s^{-1} at 1-km altitude and 25 m s^{-1} at 4-km altitude). The median vertical shear is stronger compared to both the stable and unstable storm subset cross sections of mean radial velocity for the Eureka, California, region shown in JH2005 (their Fig. 7). The difference is likely related to stronger shear within Oregon versus California storms and is at least partially attributable to smoothing of the radar data in JH2005.

Compared to U and rain-layer depth, the spatial pattern of precipitation exceedance frequency is less sensitive to variations in stability (N_m^2) in the Portland, Oregon, region (Fig. 9). The spatial patterns in frequency and intensity for <25th and >75th percentile Fr (not shown) are similar to those for U. Our sample includes only cool-season storms and the distribution of storm 12-h samples is strongly skewed to near-neutral conditions (Fig. 2). Examination of storms in the summer season would likely increase the number of unstable cases (e.g., PG2010), but this is beyond the scope of this study. A forthcoming study will address precipitation enhancement in relation to single-layer unblocked versus two-layer blocked flows and local convergence for the Portland region.

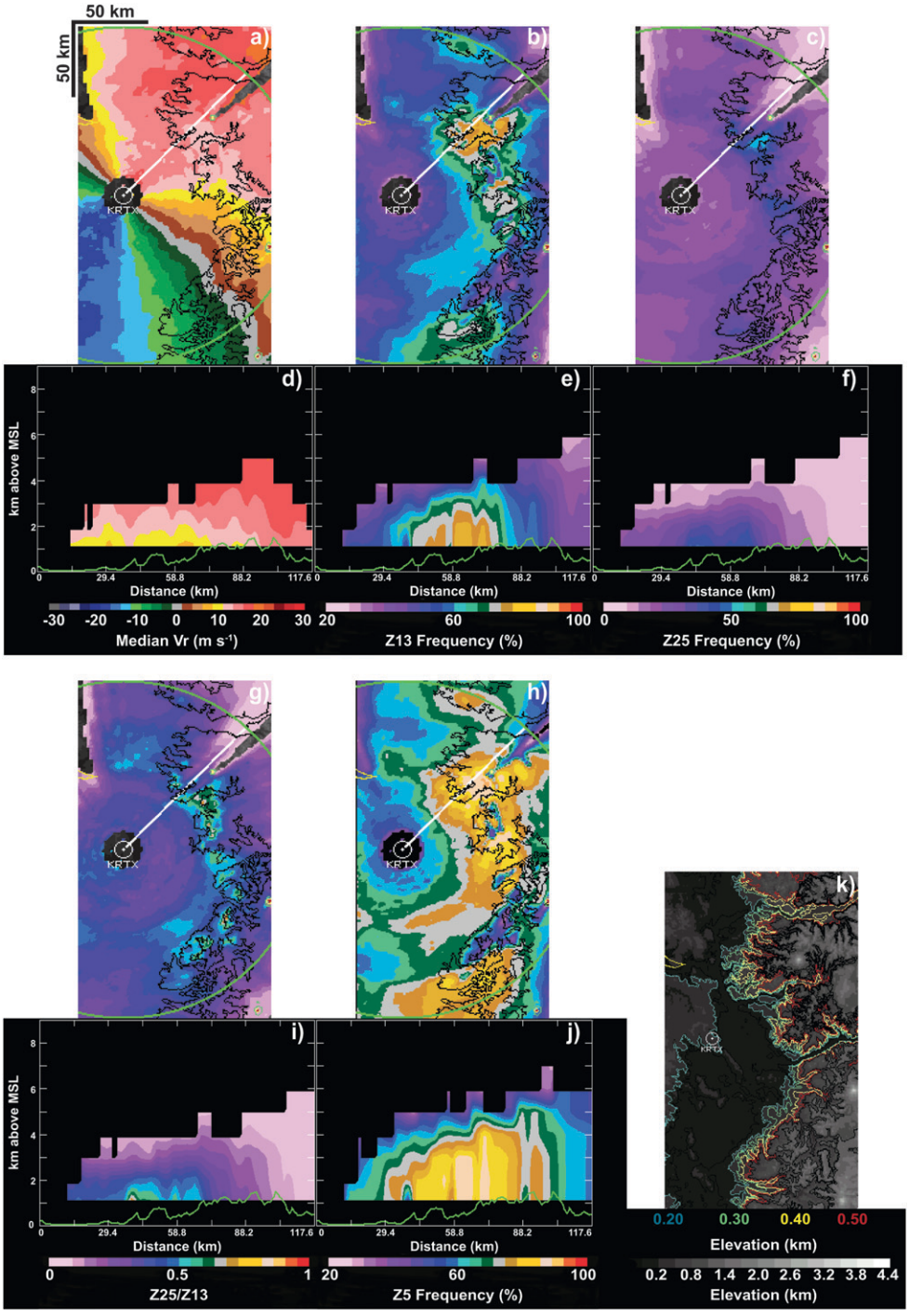

FIG. 8. Typical storm composite horizontal and vertical cross sections. Horizontal cross sections at 2-km altitude for (a) median radial velocity (Vr; m s^{-1}); (b) $Z \geq 13$ dBZ exceedance frequency (%); (c) $Z \geq 25$ dBZ exceedance frequency (%); (g) Z25/Z13 ratio (relative precipitation intensity); and (h) $Z \geq 5$ dBZ exceedance frequency (%). (k) Detailed topography for same region. Red topographic contour in (k) is the same as the single black line in (a),(b),(c),(g),(h). White radial lines in horizontal cross sections correspond to vertical cross sections: (d) median radial velocity; (e) $Z \geq 13$ dBZ exceedance frequency; (f) $Z \geq 25$ dBZ exceedance frequency; (i) Z25/Z13 ratio (relative precipitation intensity); and (j) $Z \geq 5$ dBZ exceedance frequency. Typical storm characteristics are defined as 12-h periods with wind direction U, stability, and rain-layer depth all within 25th and 75th percentiles. See Table 3, subset of 2003–06 winter 12-h periods with 198° < WDIR < 231°, for values.

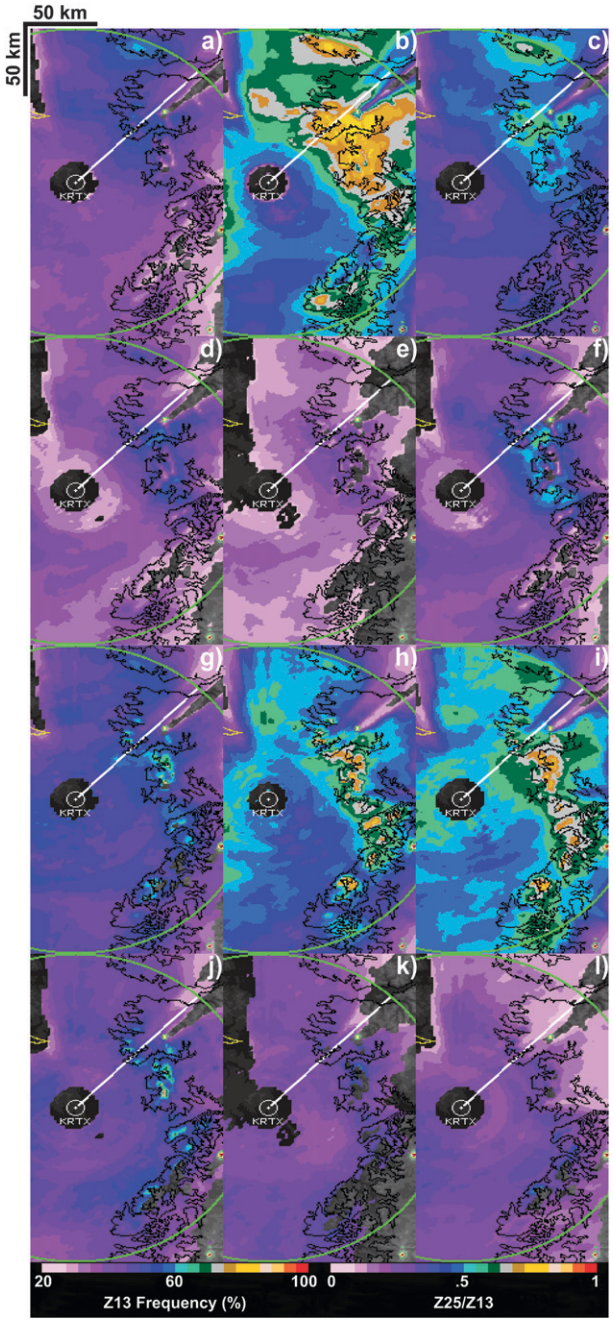

FIG. 9. Horizontal spatial patterns of radar-derived variables at 2-km altitude associated with <25th vs >75th percentile conditions of (left) N_m^2, (middle) U, and (right) 0°C level height (m); $Z \geq 13$ dBZ exceedance frequency (%) for (a)–(c) >75th percentile of variable and (d)–(f) <25th percentile of variable. Z25/Z13 ratio (relative precipitation intensity) for (g)–(i) >75th percentile of variable and (j)–(l) <25th percentile of variable. White radial lines correspond to vertical cross sections in Fig. 10.

8. Discussion

Our interpretation is that the differences in the presence and locations of high precipitation intensity in general and graupel in particular are partially a function of the 0°C level height relative to the local peaks along the windward slope. The signature of this sensitivity of the locations of locally more intense precipitation to 0°C altitude can be illustrated by comparing the 0°C level height subsets > 75th percentile, <25th percentile (Figs. 9i and 9l), and the more typical conditions (Fig. 8g). As 0°C level height increases, the locations of maximum relative intensity extend (rather than migrate) further upslope on the Cascade windward slope to the northeast of the radar. The first peak in terrain along the windward slope remains an active (but not the only) site of intense precipitation as the region of locally more intense precipitation broadens upslope.

Whether the orographic flow is blocked or unblocked is clearly important. In observational studies, differences in orographic enhancement as a function of stability are best isolated when low-level wind direction, cross-barrier wind speed, and 0°C level height are controlled for. Otherwise, these factors may dominate the observed differences.

Based on analysis of the Portland, Oregon, region storms, we infer that the schematic cross sections contrasting airflow and microphysics of unstable, unblocked, low-level flow with stable, blocked, low-level flow derived from MAP observations by Medina and Houze (2003, their Fig. 17), which were refined in Rotunno and Houze (2007, their Fig. 15), do not cleanly isolate the differences between the various stability and flow regimes. Our criticism is that variations in near-surface temperature, mixing ratio, and 0°C level height among the MAP storms, which contribute to differences in the altitude and presence of graupel, were not adequately taken into account. Medina and Houze's (2003) analysis of MAP IOP2b with a surface temperature of ~19° and 0°C level height of 3.4 km indicated graupel only above the lower slope peaks (their Fig. 12). In contrast, Pujol et al.'s (2005) examination of MAP IOP3, which had a surface temperature of 20° and 0°C level height of ~3.8 km, indicated the presence of riming and graupel above the lower slope peaks as well as peaks located further upslope (i.e., at higher altitudes, their Fig. 15).

In some previous studies, the role of U in precipitation enhancement has been camouflaged within the Froude number (e.g., Carbone et al. 1995; Medina and Houze 2003). By examining U versus N_m^2 separately, we have shown that variations in U dominate variations in N_m^2 within the Froude number in determining the degree of enhancement in orographic precipitation intensity and frequency (Figs. 4 and 9). This relative larger importance of U compared to N_m^2 for Portland is consistent with PG2010's results for the Southern Alps.

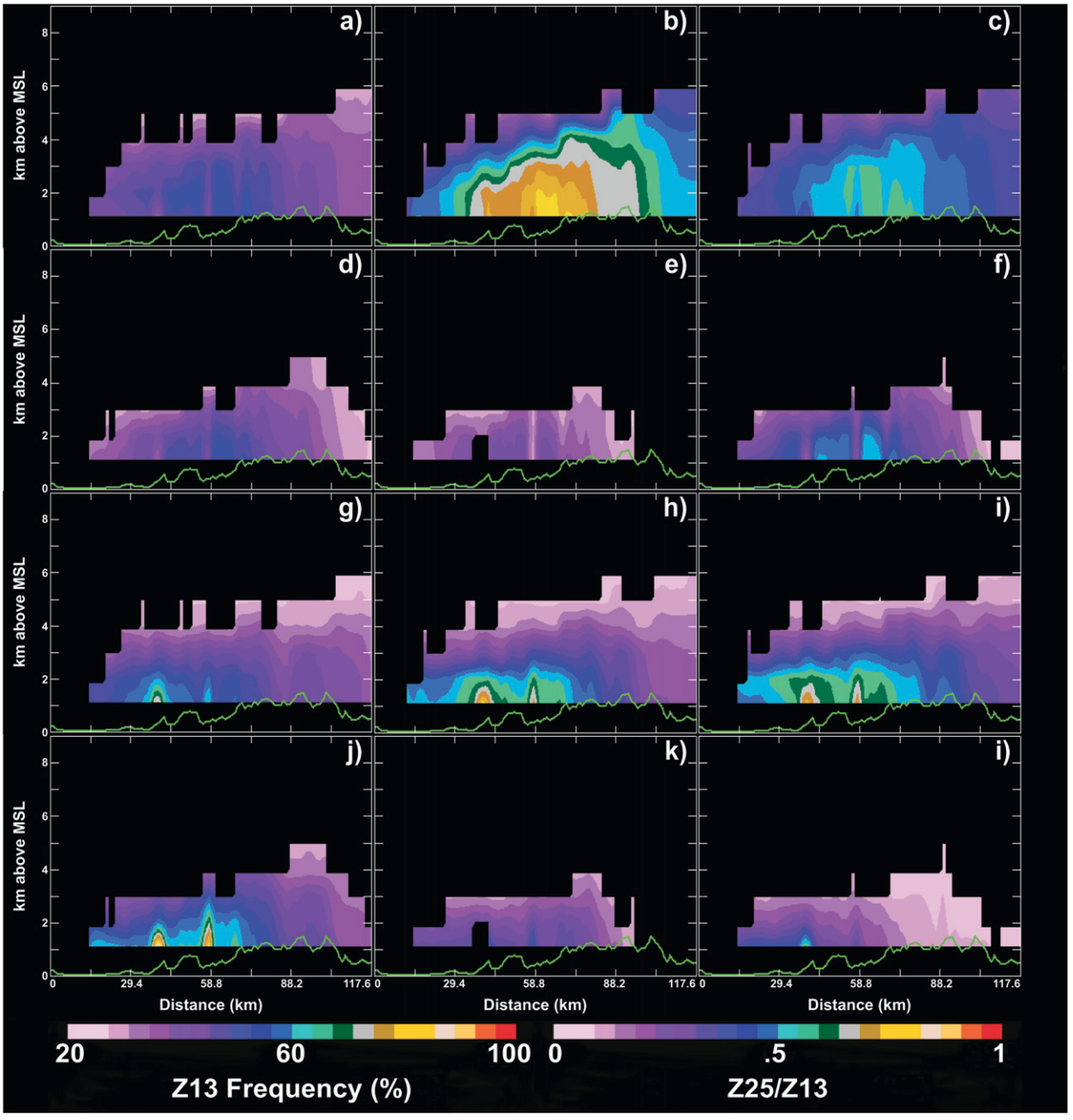

FIG. 10. Vertical cross sections of radar-derived variables along white radial lines in Fig. 9. Individual panels are shown in same order as in Fig. 9.

This observational sensitivity study complements model sensitivity studies in several ways. It documents the distributions of various environmental variables and their joint variation. With this information, modelers can focus on the subset of ranges and the joint variability of environmental conditions that actually exist in nature and are more typical for the region. While much can be learned from the study of atypically strong cross-barrier winds such as the 13–14 December 2001 IMPROVE II case, improvements to routine operational forecasts require detailed examination of more typical storms as well. A broader impact of determining the locations of precipitation frequency local maxima relates to the husbanding of limited observing instrument resources. Moving a subset of precipitation gauges to locations where precipitation is more frequent and intense may improve flood forecasting for the associated watersheds.

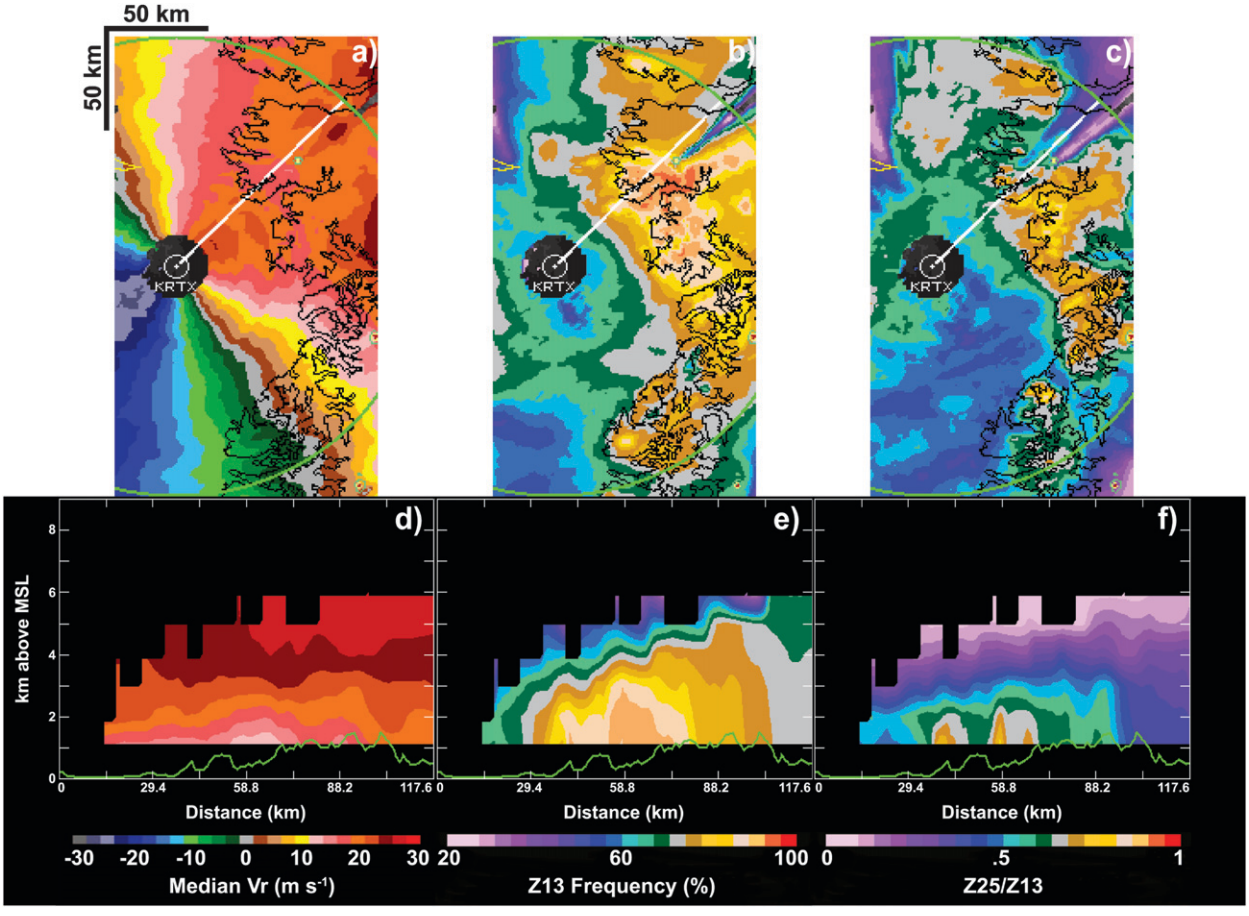

FIG. 11. Horizontal and vertical cross sections of radar-derived variables associated with wind directions between 198°–231° azimuth and $U >$ 75th percentile and 0°C level height (m) > 75th percentile. (a),(d) Median radial velocity (Vr; m s^{-1}); (b),(e) $Z \geq 13$ dBZ exceedance frequency (%); and (c),(f) Z25/Z13 ratio (relative precipitation intensity). Horizontal cross sections are at 2-km altitude, and vertical cross sections are along white lines shown in horizontal cross sections.

The small sample of storms obtained by NCAR S-band dual-polarization Doppler radar (S-POL) during IMPROVE II does not provide a contrast between unstable and stable flows for high 0°C level heights (Fig. 4). Many more storm observations with dual-polarization radar data over terrain are needed to resolve questions regarding the occurrence of graupel and should be available once operational radar networks in the United States and Europe install planned upgrades to include dual-polarization variables.

9. Conclusions

Radial velocity and radar reflectivity data from the Portland, Oregon, NWS WSR-88D radar are analyzed for 117 winter-season storms (1 November–31 March) from 2003–06 to determine the typical spatial patterns of precipitation and winds for this region and their relation to thermodynamic characteristics from the nearby NWS upper-air sounding at Salem, Oregon. The upper-air soundings are used to calculate 0°C level height and layer-averaged (1010–770 hPa) wind direction, cross-barrier wind speed, and N_m^2. We subdivide the individual storms from 2003–06 into 261 12-h periods and assume that the upper-air sounding environmental variables are reasonably representative for the period ±6 h from the upper-air sounding time.

To mitigate the impact on our analysis of variable melting-layer heights within and among storms (Medina et al. 2007), we use precipitation exceedance frequencies ≥ 13 and ≥ 25 dBZ to determine the locations and frequency of precipitation enhancement and the ratio of ≥25 dBZ to ≥13 dBZ echo to describe the relative intensity of the enhancement. Additionally, we use accumulated 3D echo volume per hour for reflectivities ≥ 13 dBZ and for ≥ 25 dBZ as measures of storm scale that combines information on the horizontal geographic extent, vertical extent, and frequency of the storm. Since the distributions of most of the observed variables were

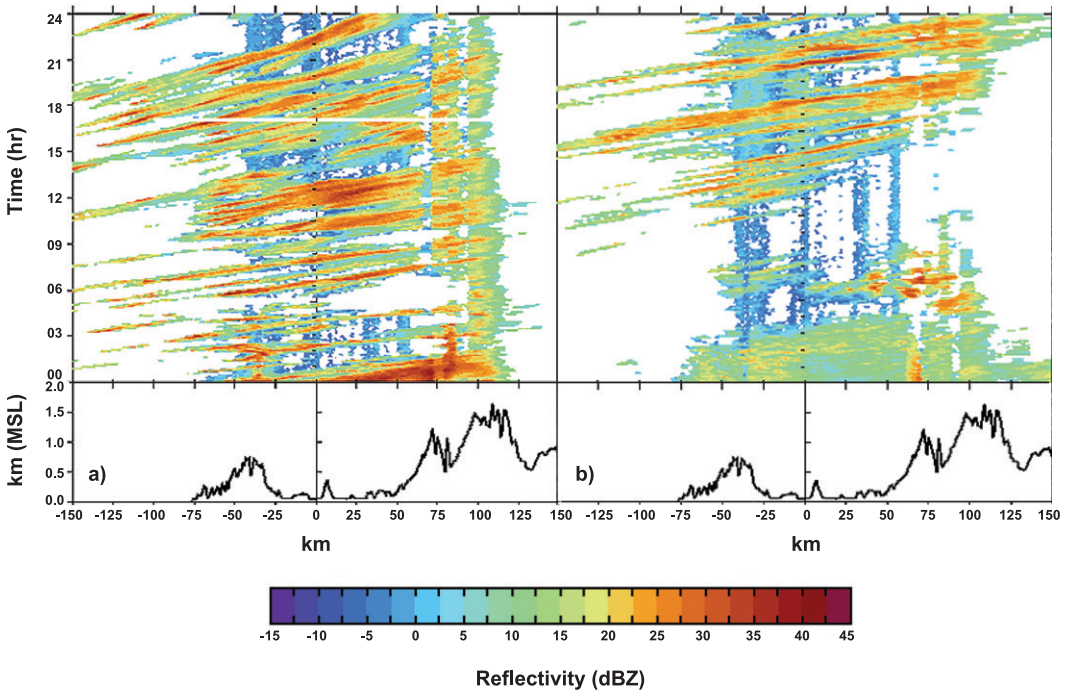

FIG. 12. Hovmöller plots of radar reflectivity at 2 km MSL for a west–east section at 42.35°N latitude. (a) High U and low 0°C level for 9 Mar 2006 storm (12-h sounding U = 20.4, 14.1 m s^{-1}; 0°C level height = 1.0 and 0.35 km). (b) Low U and low 0°C level for 29 Nov 2005 storm (12-h sounding U = 5.6 m s^{-1}; 0°C level height = 0.94 km). (bottom) Topography along 42.35°N latitude is shown. Figure courtesy of Yanluan Lin.

non-Gaussian (Fig. 2), we use percentiles to characterize the distributions rather than means and standard deviations because percentiles are less sensitive to outliers (Taleb 2007). The distribution of observed storm volumes is strongly skewed toward smaller volumes (Fig. 3).

The larger sample size of storms in this study helps to place the IMPROVE II field project dataset into context. The IMPROVE II storms sample a wide range of cross-barrier wind speeds for freezing-level heights near 1-km altitude but include only a few samples with freezing-level height higher than 1.5-km altitude. More of the IMPROVE II storm periods had wind directions outside the 25th to 75th percentiles than inside, thus yielding a sample that is climatologically unrepresentative for wind direction. The well-studied 13–14 December 2001 IMPROVE II storm is an outlier case: 99% of 12-h periods examined had lower layer-average cross-barrier wind speed.

Consistent with other observational studies (Frei and Schär 1998; Houze et al. 2001; Ralph et al. 2003; JH2005; PG2010), wind direction has a dominant role in determining the geographic pattern of precipitation in the Portland, Oregon, region (Fig. 7), with mountain slopes roughly perpendicular to the local flow receiving the most frequent precipitation. We use a subset of 129 12-h storm periods with winds from 198°–231° azimuth (corresponding to the 25th and 75th percentiles) to examine the sensitivity of the spatial pattern of precipitation to differences in stability, cross-barrier wind speed, and rain-layer depth (Figs. 4, 5, and 6; Table 4). As a rough analog to model sensitivity studies, we contrast the precipitation exceedance frequencies for the <25th percentile subsample with the >75th percentile subsample for each environmental variable and compare these to the typical case (25th to 75th percentile subsample). Use of the narrow wind direction subset allows us to isolate the sensitivity to environmental conditions without the muddling influence of different spatial patterns of precipitation associated with different wind directions. Cross-barrier wind speed and 0°C level height in our storm sample are essentially independent (Fig. 4), allowing us to explore their joint sensitivity to precipitation pattern.

Local maxima in the maps of precipitation frequency and intensity are primarily a function of the local low-level wind direction and the 3D geometry of the terrain and secondarily a function of other environmental conditions. Precipitation enhancement relative to local peaks in terrain along the windward slope is highly sensitive to both the particular cross section viewed and the precipitation exceedance threshold used.

For a given environment, the frequency and intensity patterns of precipitation over the windward slope of the Cascades overlap but differ in the spatial extent and locations of maxima. The roles of variations in U and 0°C

level height differ for precipitation frequency versus precipitation intensity. The >75th percentile U subset dominates the >75th percentile 0°C level height subset in the magnitude of precipitation frequency (Figs. 9b, 9c, 10b, and 10c). In contrast, the >75th percentile subsets of U and rain-layer depth are more comparable for precipitation intensity with rain-layer depth having a slightly stronger role (Figs. 9h, 9i, 10h, and 10i). The increase in precipitation frequency with stronger U is partially attributed to the higher wind speeds increasing the flux of preexisting convective cells intersecting the windward slope. The area where inferred riming growth and associated higher rain rates occur over local peaks on the windward slope broadens upslope as the 0°C level height increases. Compared to U and rain-layer depth, the spatial pattern of precipitation is less sensitive to variations in stability (in terms of N_m^2) in the Portland, Oregon, region. This result may be a consequence of the distribution of stability within our sample of winter storms, which is strongly skewed to near neutral conditions (Fig. 2).

The sensitivity of orographic precipitation to cross-barrier wind speed is well known from both modeling and empirical studies (e.g., Smith and Barstad 2004; Colle 2004; PG2010). The importance of the 0°C level height in the rainfall accumulation over a windward slope has been previously recognized in climatologies of U.S. west coast flooding events (Ralph et al. 2003; Lundquist et al. 2008; Neiman et al. 2008). In the Portland region, deep rain layers and high cross-barrier winds combine to yield a large horizontal area along the windward slope with precipitation exceedance frequencies > 70% (Fig. 11). This joint subset is more frequently associated with larger storm echo volumes than other combinations of rain-layer depth and cross-barrier wind speed (Fig. 4f).

Acknowledgments. Special thanks to Kimberly Comstock, Jeffrey Cunningham, Tim Downing, David Kingsmill, Yanluan Lin, Matthew A. Miller, Marc Michelson, Dave Spencer, Catherine Spooner, and Karl Wegmann for advice and technical help. We thank Socorro Medina and three anonymous reviewers for their constructive comments that helped improve the paper. Christina Cartwright edited the manuscript. This material is based upon work supported by the National Science Foundation under Grant Numbers ATM-0544766 (Yuter) and ATM-0450444 (Colle). Any opinions, findings, and conclusions or recommendations expressed in this material are those of the author(s) and do not necessarily reflect the views of the National Science Foundation.

REFERENCES

Austin, P. M., 1987: Relation between measured radar reflectivity and surface rainfall. *Mon. Wea. Rev.,* **115,** 1053–1070.

Bao, J.-W., S. A. Michelson, P. J. Neiman, F. M. Ralph, and J. M. Wilczak, 2006: Interpretation of enhanced integrated water-vapor bands associated with extratropical cyclones: Their formation and connection to tropical moisture. *Mon. Wea. Rev.,* **134,** 1063–1080.

Barnes, S. L., 1980: Report on a meeting to establish a common Doppler radar data exchange format. *Bull. Amer. Meteor. Soc.,* **61,** 1401–1404.

Battan, L. J., 1973: *Radar Observation of the Atmosphere*. University of Chicago Press, 324 pp.

Bougeault, P., and Coauthors, 2001: The MAP special observing period. *Bull. Amer. Meteor. Soc.,* **82,** 433–462.

Braham, R. R., 1964: What is the role of ice in summer rain showers? *J. Atmos. Sci.,* **21,** 640–645.

Carbone, R. E., W. A. Cooper, and W.-C. Lee, 1995: Forcing of flow reversal along the windward slopes of Hawaii. *Mon. Wea. Rev.,* **123,** 3466–3480.

Castello, A. F., and M. L. Shelton, 2004: Winter precipitation on the U.S. Pacific coast and El Niño–Southern Oscillation Events. *Int. J. Climatol.,* **24,** 481–497.

Cayan, D. R., and J. O. Roads, 1984: Local relationships between U.S. West Coast precipitation and monthly mean circulation parameters. *Mon. Wea. Rev.,* **112,** 1276–1282.

Colle, B. A., 2004: Sensitivity of orographic precipitation to changing ambient conditions and terrain geometries: An idealized modeling perspective. *J. Atmos. Sci.,* **61,** 588–606.

——, 2008: Two-dimensional idealized simulations of the impact of multiple windward ridges on orographic precipitation. *J. Atmos. Sci.,* **65,** 509–523.

——, and C. F. Mass, 2000: The 5–9 February 1996 flooding event over the Pacific Northwest: Sensitivity studies and evaluation of the MM5 precipitation forecasts. *Mon. Wea. Rev.,* **128,** 593–617.

——, M. F. Garvert, J. B. Wolfe, C. F. Mass, and C. P. Woods, 2005a: The 13–14 December 2001 IMPROVE-2 event. Part III: Simulated microphysical budgets and sensitivity studies. *J. Atmos. Sci.,* **62,** 3535–3558.

——, J. B. Wolfe, W. J. Steenburgh, D. E. Kingsmill, J. A. W. Cox, and J. C. Shafer, 2005b: High-resolution simulations and microphysical validation of an orographic precipitation event over the Wasatch Mountains during IPEX IOP3. *Mon. Wea. Rev.,* **133,** 2947–2971.

——, Y. Lin, S. Medina, and B. F. Smull, 2008: Orographic modification of convection and flow kinematics by the Oregon Coast Range and Cascades during IMPROVE-2. *Mon. Wea. Rev.,* **136,** 3894–3916.

Daly, C., R. P. Neilson, and D. L. Phillips, 1994: A statistical-topographic model for mapping climatological precipitation over mountainous terrain. *J. Appl. Meteor.,* **33,** 140–158.

Doyle, J. D., and Q. Jiang, 2006: Observations and numerical simulations of mountain waves in the presence of directional wind shear. *Quart. J. Roy. Meteor. Soc.,* **132,** 1877–1905.

Durran, D. R., and J. B. Klemp, 1982: On the effects of moisture on the Brunt–Väisälä frequency. *J. Atmos. Sci.,* **39,** 2152–2158.

Frei, C., and C. Schär, 1998: A precipitation climatology of the Alps from high-resolution rain gauge observations. *Int. J. Climatol.,* **18,** 873–900.

Galewsky, J., and A. Sobel, 2005: Moist dynamics and orographic precipitation in northern and central California during the New Year's flood of 1997. *Mon. Wea. Rev.,* **133,** 1594–1612.

Garvert, M. F., B. A. Colle, and C. F. Mass, 2005a: The 13–14 December 2001 IMPROVE-2 event. Part I: Synoptic and mesoscale evolution and comparison with a mesoscale model simulation. *J. Atmos. Sci.,* **62,** 3474–3492.

——, C. P. Woods, B. A. Colle, C. F. Mass, P. V. Hobbs, M. T. Stoelinga, and J. B. Wolfe, 2005b: The 13–14 December 2001 IMPROVE-2 event. Part II: Comparisons of MM5 model simulations of clouds and precipitation with observations. *J. Atmos. Sci.,* **62,** 3520–3534.

——, B. Smull, and C. Mass, 2007: Multiscale mountain waves influencing a major orographic precipitation event. *J. Atmos. Sci.,* **64,** 711–737.

Guirguis, K. J., and R. Avissar, 2008: A precipitation climatology and dataset intercomparison for the western United States. *J. Hydrometeor.,* **9,** 825–841.

Hagen, M., and S. E. Yuter, 2003: Relation between radar reflectivity and rainfall rate during the MAP-SOP. *Quart. J. Roy. Meteor. Soc.,* **129,** 477–493.

Hamlet, A. F., and D. P. Lettenmaier, 2007: Effects of 20th century warming and climate variability on flood risk in the western U.S. *Water Resour. Res.,* **43,** W06427, doi:10.1029/2006WR005099.

Houze, R. A., Jr., and S. Medina, 2005: Turbulence as a mechanism for orographic precipitation enhancement. *J. Atmos. Sci.,* **62,** 3599–3623.

——, C. N. James, and S. Medina, 2001: Radar observations of precipitation and airflow on the Mediterranean side of the Alps: Autumn 1998 and 1999. *Quart. J. Roy. Meteor. Soc.,* **127,** 2537–2558.

Hughes, M., A. Hall, and R. G. Fovell, 2009: Blocking in areas of complex topography, and its influence on rainfall distributions. *J. Atmos. Sci.,* **66,** 508–518.

James, C. N., and R. A. Houze Jr., 2001: A real-time four-dimensional Doppler dealiasing scheme. *J. Atmos. Oceanic Technol.,* **18,** 1674–1683.

——, and ——, 2005: Modification of precipitation by coastal orography in storms crossing northern California. *Mon. Wea. Rev.,* **133,** 3110–3131.

——, S. R. Brodzik, H. Edmon, R. A. Houze Jr., and S. E. Yuter, 2000: Radar data processing and visualization over complex terrain. *Wea. Forecasting,* **15,** 327–338.

Jiang, Q., 2003: Moist dynamics and orographic precipitation. *Tellus,* **55,** 301–316.

Johnson, D. B., 1987: On the relative efficiency of coalescence and riming. *J. Atmos. Sci.,* **44,** 1671–1680.

Joss, J., and Coauthors, 1998: *Operational Use of Radar for Precipitation Measurements in Switzerland*. vdf Hochschulverlag AG an der ETH Zürich, 108 pp.

Kalnay, E., and Coauthors, 1996: The NCEP/NCAR 40-Year Reanalysis Project. *Bull. Amer. Meteor. Soc.,* **77,** 437–471.

Kirshbaum, D. J., and D. R. Durran, 2005: Atmospheric factors governing banded orographic convection. *J. Atmos. Sci.,* **62,** 3758–3774.

Krajewski, W. F., and J. A. Smith, 2002: Radar hydrology: Rainfall estimation. *Adv. Water Resour.,* **25,** 1387–1394.

Kunz, M., and C. Kottmeier, 2006: Orographic enhancement of precipitation over low mountain ranges. Part I: Model formulation and idealized simulations. *J. Appl. Meteor. Climatol.,* **45,** 1025–1040.

Lackmann, G. M., and J. R. Gyakum, 1999: Heavy cold-season precipitation in the northwestern United States: Synoptic climatology and an analysis of the flood of 17–18 January 1986. *Wea. Forecasting,* **14,** 687–700.

Lundquist, J. D., P. J. Neiman, B. Martner, A. B. White, D. J. Gottas, and F. M. Ralph, 2008: Rain versus snow in the Sierra Nevada, California: Comparing Doppler profiling radar and surface observations of the melting level. *J. Hydrometeor.,* **9,** 194–211.

Medina, S., and R. A. Houze Jr., 2003: Air motions and precipitation growth in Alpine storms. *Quart. J. Roy. Meteor. Soc.,* **129,** 345–371.

——, B. F. Smull, R. A. Houze Jr., and M. Steiner, 2005: Cross-barrier flow during orographic precipitation events: Results from MAP and IMPROVE. *J. Atmos. Sci.,* **62,** 3580–3598.

——, E. Sukovich, and R. A. Houze Jr., 2007: Vertical structures of precipitation in cyclones crossing the Oregon Cascades. *Mon. Wea. Rev.,* **135,** 3565–3586.

Miglietta, M. M., and R. Rotunno, 2006: Further results on moist nearly neutral flow over a ridge. *J. Atmos. Sci.,* **63,** 2881–2897.

Minder, J. R., D. R. Durran, G. H. Roe, and A. M. Anders, 2008: The climatology of small-scale orographic precipitation over the Olympic Mountains: Patterns and processes. *Quart. J. Roy. Meteor. Soc.,* **134,** 817–839.

Neiman, P. J., P. O. G. Persson, F. M. Ralph, D. P. Jorgensen, A. B. White, and D. E. Kingsmill, 2004: Modification of fronts and precipitation by coastal blocking during an intense landfalling winter storm in Southern California: Observations during CALJET. *Mon. Wea. Rev.,* **132,** 242–273.

——, F. M. Ralph, G. A. Wick, J. D. Lundquist, and M. D. Dettinger, 2008: Meteorological characteristics and overland precipitation impacts of atmospheric rivers affecting the west coast of North America based on eight years of SSM/I satellite observations. *J. Hydrometeor.,* **9,** 22–47.

Panziera, L., and U. Germann, 2010: The relationship between airflow and orographic precipitation in the Southern Alps as revealed by weather radar. *Quart. J. Roy. Meteor. Soc.,* **136,** 222–238.

Praskievicz, S., and H. Chang, 2009: Winter precipitation intensity and ENSO/PDO variability in the Willamette Valley of Oregon. *Int. J. Climatol.,* **29,** 2033–2039.

Pujol, O., J. F. Georgis, M. Chong, and F. Roux, 2005: Dynamics and microphysics of orographic precipitation during MAP IOP 3. *Quart. J. Roy. Meteor. Soc.,* **131,** 2795–2819.

Ralph, F. M., P. J. Neiman, D. E. Kingsmill, P. O. G. Persson, and A. B. White, 2003: The impact of a prominent rain shadow on flooding in California's Santa Cruz Mountains: A CALJET case study and sensitivity to the ENSO cycle. *J. Hydrometeor.,* **4,** 1243–1264.

——, ——, and G. A. Wick, 2004: Satellite and CALJET aircraft observations of atmospheric rivers over the eastern North Pacific Ocean during the winter of 1997/98. *Mon. Wea. Rev.,* **132,** 1721–1745.

——, ——, and R. Rotunno, 2005: Dropsonde observations in low-level jets over the northeastern Pacific Ocean from CALJET-1998 and PACJET-2001: Mean vertical-profile and atmospheric-river characteristics. *Mon. Wea. Rev.,* **133,** 889–910.

Reeves, H. D., and Y. L. Lin, 2008: Dynamic forcing and mesoscale variability of heavy precipitation events over the Sierra Nevada Mountains. *Mon. Wea. Rev.,* **136,** 62–77.

Reinecke, P. A., and D. R. Durran, 2008: Estimating topographic blocking using a Froude number when the static stability is nonuniform. *J. Atmos. Sci.,* **65,** 1035–1048.

Rotunno, R., and R. Ferretti, 2001: Mechanisms of intense Alpine rainfall. *J. Atmos. Sci.,* **58,** 1732–1749.

——, and R. A. Houze Jr., 2007: Lessons on orographic precipitation from the Mesoscale Alpine Programme. *Quart. J. Roy. Meteor. Soc.,* **133,** 811–830.

Seo, D. J., J. Breidenback, R. Fulton, and D. Miller, 2000: Real-time adjustment of range-dependent biases in WSR-88D rainfall estimates due to nonuniform vertical profile of reflectivity. *J. Hydrometeor.,* **1,** 222–240.

Sharp, J., and C. F. Mass, 2004: Columbia Gorge gap winds: Their climatological influence and synoptic evolution. *Wea. Forecasting,* **19,** 970–992.

Smith, R. B., 1979: The influence of mountains on the atmosphere. *Advances in Geophysics,* Vol. 21, Academic Press, 87–230.

——, 2003: A linear upslope-time-delay model for orographic precipitation. *J. Hydrol.,* **282,** 2–9.

——, 2006: Progress on the theory of orographic precipitation. *Tectonics, Climate and Landscape Evolution: Geological Society of America Special Paper 398,* S. D. Willett et al., Eds., Penrose Conference Series, 1–16.

——, and I. Barstad, 2004: A linear theory of orographic precipitation. *J. Atmos. Sci.,* **61,** 1377–1391.

——, Q. Jiang, M. G. Fearon, P. Tabary, M. Dorninger, J. D. Doyle, and R. Benoit, 2003: Orographic precipitation and air mass transformation: An Alpine example. *Quart. J. Roy. Meteor. Soc.,* **129,** 433–454.

——, I. Barstad, and L. Bonneau, 2005: Orographic precipitation and Oregon's climate transition. *J. Atmos. Sci.,* **62,** 177–191.

Stoelinga, M. T., and Coauthors, 2003: Improvement of Microphysical Parameterization through Observational Verification Experiment (IMPROVE). *Bull. Amer. Meteor. Soc.,* **84,** 1807–1826.

Taleb, N. N., 2007: *The Black Swan: The Impact of the Highly Improbable*. Random House, 366 pp.

Tanré, D., P. Artuxo, S. Yuter, and Y. Kaufman, 2008: In situ and remote sensing techniques for measuring aerosols, clouds, and precipitation. *Aerosol Pollution Impacts on Precipitation: A Scientific Review,* Springer, 143–203.

Westrick, K. J., C. F. Mass, and B. A. Colle, 1999: The limitations of the WSR-88D radar network for quantitative precipitation measurement over the coastal western United States. *Bull. Amer. Meteor. Soc.,* **80,** 2289–2298.

White, A. B., P. J. Neiman, F. M. Ralph, D. E. Kingsmill, and P. O. G. Persson, 2003: Coastal orographic rainfall processes observed by radar during the California Land-Falling Jets Experiment. *J. Hydrometeor.,* **4,** 264–282.

Yuter, S. E., 2002: Precipitation radar. *Encyclopedia of Atmospheric Sciences,* J. Holton et al., Eds., Academic Press, 1833–1852.

——, D. Kingsmill, L. B. Nance, and M. Löffler-Mang, 2006: Observations of precipitation size and fall speed characteristics within coexisting rain and wet snow. *J. Appl. Meteor. Climatol.,* **45,** 1450–1464.

Zängl, G., 2008: The temperature dependence of small-scale orographic precipitation enhancement. *Quart. J. Roy. Meteor. Soc.,* **134,** 1167–1181.

Zhu, Y., and R. E. Newell, 1998: A proposed algorithm for moisture fluxes from atmospheric rivers. *Mon. Wea. Rev.,* **126,** 725–735.